



L2A+

Ref: Ref: ESA AO/1-11041/22/I-NS

DI05: Output Data Product (OP)

Page: 1

L2A+

# Enhanced Aeolus L2A for depolarizing targets and impact on aerosol research and NWP

-

Output Data Product  
(OP)

Deliverable Item 05  
[DI05]  
(Final Version - FV)

Submitted to: Edward Malina (ESA)

|              | Name          | Function               | Date    |
|--------------|---------------|------------------------|---------|
| Prepared by: | E. Proestakis | WP1000 – NOA           | 11/2024 |
|              | K. Rizos      | WP3000 – NOA           | 11/2024 |
|              | A. Gkikas     | WP3000 – NOA           | 11/2024 |
|              | A. A. Floutsi | WP2000 – TROPOS        | 11/2024 |
| Approved by: | H. Baars      | WP2000 – TROPOS – CoPI | 11/2024 |
|              | V. Amiridis   | PI                     | 11/2024 |

-

National Observatory of Athens (NOA)  
Institute for Astronomy, Astrophysics, Space Applications & Remote Sensing (IAASARS)  
Vas. Pavlou & I. Metaxa, 15236 Penteli, Greece

&

Leibniz Institute for Tropospheric Research (TROPOS), Leipzig, Germany

&

European Centre for Medium-Range Weather Forecasts  
[ ECMWF ]

Reading, United Kingdom

*ESA-L2A+ Deliverable Item 05 [DI05]*



*L2A+*

Ref: *Ref: ESA AO/1-11041/22/I-NS*

DI05: Output Data Product (OP)

Page: 2

[This page is intentionally left blank.]



# L2A+

Ref: *Ref: ESA AO/1-11041/22/I-NS*

DI05: Output Data Product (OP)

Page: 3

## Table of Contents

|   |    |
|---|----|
| 1. ESA-L2A+ DI05 – Overview. ....   | 4  |
| 2. Unique feature mask over Mindelo and PollyXT optical properties .....                      | 5  |
| 2.1. Unique feature mask over Mindelo. ....   | 5  |
| 2.2. PollyXT optical properties.....  | 8  |
| 2.3. Access Credentials .....   | 20 |
| 2.4. Contact Person. ....   | 20 |
| 3. The L2A+ Product.....  | 21 |
| 3.1. Introduction.....  | 21 |
| 3.2. Filename Format .....  | 21 |
| 3.3. Indicative Study-Case: The Aeolus-Cabo Verde overpass on the 10th of September 2021 .... | 21 |
| 3.3.1. Description of the atmospheric scene. ....   | 21 |
| 3.3.5. L2A+ - ESA-PollyXT validation .....  | 29 |
| 3.4. The L2A+ products.....   | 31 |
| 3.5. Access Credentials .....   | 51 |
| 3.6. Contact Person .....   | 51 |
| Acronyms and Abbreviations.....   | 52 |
| List of Figures .....   | 52 |
| List of Tables .....  | 54 |



## 1. ESA-L2A+ DI05 – Overview.

This document consists the Deliverable Item 05 (DI05) – Optical Products “OPs” – Final Version (FV) submitted to the European Space Agency (ESA) by the consortium of the project “Enhanced Aeolus L2A for depolarizing targets and impact on aerosol research and NWP” (L2A+). DI05– OPs reports on the (1) filenames, (2) variables, (3) access credentials, and (4) contact persons of L2A+ WP2000 – “ASKOS ground-based datasets in support of L2A+” and WP3000 – “Development of the L2A+ aerosol product” and WP4000 – “Development of the L2A+ aerosol product” output product datasets (Figure 1).

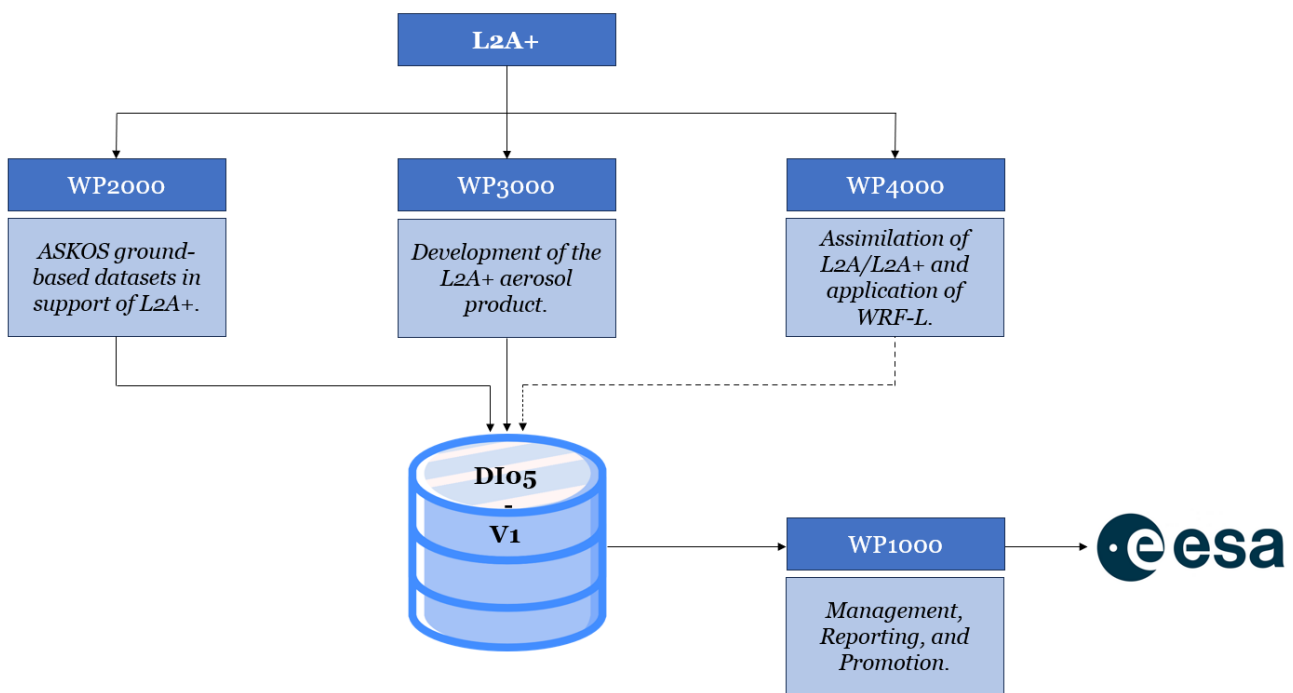


Figure 1: ESA-L2A+ WP2000, WP3000, and WP4000 input and outputs relevant to DI05.



## 2. Unique feature mask over Mindelo and PollyXT optical properties

### 2.1. Unique feature mask over Mindelo.

The unique height-resolved feature mask utilizes lidar, cloud radar and microwave radiometer data and allows for high-performance cloud and feature detection (Combined Cloudnet + EARLINET lidar target categorization).

The filenames follow the structure: “YYYYMMDD\_regridded\_data\_for\_mindelo.nc”

Table 1: Provides the vertical profiles of the co-component of backscatter coefficient along the Aeolus overpass.

| Group              | Subgroup | Variable                          | Units              | Dimensions | Description  |
|--------------------|----------|-----------------------------------|--------------------|------------|--|
| FEATURE MASK       | -        | cloudnet_LWP                      | g/m <sup>2</sup>   | 1D         | Liquid water path                                  |
|                    |          | cloudnet_radar_gas_attenuation    | dB                 | 2D         | Two-way radar attenuation due to atmospheric gases |
|                    |          | cloudnet_radar_liquid_attenuation | dB                 | 2D         | Two-way radar attenuation due to liquid water      |
|                    |          | cloudnet_radar_v                  | m/s                | 2D         | Doppler velocity                                   |
|                    |          | cloudnet_radar_width              | m/s                | 2D         | Spectral width                                     |
|                    |          | cloudnet_radar_Z                  | dBZ                | 2D         | Radar reflectivity factor                          |
|                    |          | cloudnet_radar_Z_error            | dB                 | 2D         | Error in radar reflectivity factor                 |
|                    |          | cloudnet_target_classification    | -                  | 2D         | Target classification                              |
|                    |          | combined_target_classification    | -                  | 2D         | Target classification                              |
|                    |          | height                            | m                  | 1D         | Height above mean sea level                        |
|                    |          | model_pressure                    | Pa                 | 2D         | Pressure   |
|                    |          | model_temperature                 | K                  | 2D         | Temperature  |
| polly_ang_532_1064 | -        | 2D                                | Quasi backscatter- |            |  |



|  |  |                                 |                                     |    |   |
|--|--|---------------------------------|-------------------------------------|----|---|
|  |  |                                 |                                     |    | related Ångström exponent at 532-1064 nm          |
|  |  | polly_att_bsc_1064              | sr <sup>-1</sup><br>m <sup>-1</sup> | 2D | Attenuated backscatter at 1064 nm                 |
|  |  | polly_att_bsc_532               | sr <sup>-1</sup><br>m <sup>-1</sup> | 2D | Attenuated backscatter at 532 nm                  |
|  |  | polly_bsc_1064                  | sr <sup>-1</sup><br>m <sup>-1</sup> | 2D | Quasi aerosol backscatter coefficients at 1064 nm |
|  |  | polly_bsc_1064_quality_flag     | -                                   | 2D | QC information                                    |
|  |  | polly_bsc_532                   | sr <sup>-1</sup><br>m <sup>-1</sup> | 2D | Quasi aerosol backscatter coefficients at 532 nm  |
|  |  | polly_bsc_532_quality_flag      | -                                   | 2D | QC information                                    |
|  |  | polly_pardepol_532              | -                                   | 2D | quasi particle depolarization ratio at 532 nm     |
|  |  | polly_target_classification     | -                                   | 2D | Target classification                             |
|  |  | polly_voldepol_532              | -                                   | 2D | Volume depolarization ratio at 532 nm             |
|  |  | polly_voldepol_532_quality_flag | -                                   | 2D | QC information                                    |
|  |  | time                            | UTC                                 | 1D | Hours of day                                      |



# L2A+

Ref: *Ref: ESA AO/1-11041/22/I-NS*

DI05: Output Data Product (OP)

Page: 7

| Name                                   | Long Name   | Type       |
|--|---|------------|
| 20210909_regridded_data_for_mindelo.nc | 20210909_regridded_data_for_mindelo.nc                  | Local File |
| cloudnet_LWP                           | Liquid water path                                       | 1D         |
| cloudnet_radar_gas_attenuation         | Two-way radar attenuation due to atmospheric gases      | 2D         |
| cloudnet_radar_liquid_attenuation      | Two-way radar attenuation due to liquid water           | 2D         |
| cloudnet_radar_v                       | Doppler velocity  | 2D         |
| cloudnet_radar_width                   | Spectral width  | 2D         |
| cloudnet_radar_Z                       | Radar reflectivity factor                               | 2D         |
| cloudnet_radar_Z_error                 | Error in radar reflectivity factor                      | 2D         |
| cloudnet_target_classification         | Target classification                                   | 2D         |
| combined_target_classification         | Target classification                                   | 2D         |
| height                                 | Height Axis   | 1D         |
| model_pressure                         | Pressure  | 2D         |
| model_temperature                      | Temperature   | 2D         |
| polly_ang_532_1064                     | quasi backscatter-related angstrom exponent at 532-1064 | 2D         |
| polly_att_bsc_1064                     | attenuated backscatter at 1064 nm                       | 2D         |
| polly_att_bsc_532                      | attenuated backscatter at 532 nm                        | 2D         |
| polly_bsc_1064                         | quasi aerosol backscatter coefficients at 1064 nm       | 2D         |
| polly_bsc_1064_quality_flag            | polly bsc 1064 quality flag                             | 2D         |
| polly_bsc_532                          | quasi aerosol backscatter coefficients at 532 nm        | 2D         |
| polly_bsc_532_quality_flag             | polly bsc 532 quality flag                              | 2D         |
| polly_pardepol_532                     | quasi particle depolarization ratio at 532 nm           | 2D         |
| polly_target_classification            | Target classification                                   | 2D         |
| polly_voldepol_532                     | volume depolarization ratio at 532 nm                   | 2D         |
| polly_voldepol_532_quality_flag        | polly voldepol 532 quality flag                         | 2D         |
| time                                   | Time Axis   | 1D         |

Figure 2: Indicative file output of Unique feature mask over Mindelo.



## 2.2. PollyXT optical properties.

The dataset includes vertically-resolved aerosol optical properties derived from the PollyXT ground-based, multiwavelength, Raman, polarization lidar measurements.

The filenames follow the structure:

“YYYY\_MM\_DD\_weekday\_CPV\_HH\_MM\_SS\_HHMM\_HHMM\_profiles.nc”

Table 2: Detailed description of the variables within the PollyXT profile product.

| Group               | Subgroup | Variable            | Units                            | Dimensions | Description  |
|---------------------|----------|---------------------|----------------------------------|------------|--|
| PollyXT<br>PROFILES | -        | aerBsc_aeronet_1064 | sr <sup>-1</sup> m <sup>-1</sup> | 1D         | Aerosol backscatter coefficient at 1064 nm retrieved with constrained-AOD method |
|                     |          | aerBsc_aeronet_355  | sr <sup>-1</sup> m <sup>-1</sup> | 1D         | Aerosol backscatter coefficient at 355 nm retrieved with constrained-AOD method  |
|                     |          | aerBsc_aeronet_532  | sr <sup>-1</sup> m <sup>-1</sup> | 1D         | Aerosol backscatter coefficient at 532 nm retrieved with constrained-AOD method  |
|                     |          | aerBsc_klett_1064   | sr <sup>-1</sup> m <sup>-1</sup> | 1D         | Aerosol backscatter coefficient at 1064 nm retrieved with Klett method           |
|                     |          | aerBsc_klett_355    | sr <sup>-1</sup> m <sup>-1</sup> | 1D         | Aerosol backscatter coefficient at 355 nm retrieved                              |



# L2A+

|  |  |                   |                                |    |   |
|--|--|-------------------|--------------------------------|----|---|
|  |  |                   |                                |    | with Klett method   |
|  |  | aerBsc_klett_532  | $\text{sr}^{-1} \text{m}^{-1}$ | 1D | Aerosol backscatter coefficient at 532 nm retrieved with Klett method           |
|  |  | aerBsc_raman_1064 | $\text{sr}^{-1} \text{m}^{-1}$ | 1D | Aerosol backscatter coefficient at 1064 nm retrieved with Raman method          |
|  |  | aerBsc_raman_355  | $\text{sr}^{-1} \text{m}^{-1}$ | 1D | Aerosol backscatter coefficient at 355 nm retrieved with Raman method           |
|  |  | aerBsc_raman_532  | $\text{sr}^{-1} \text{m}^{-1}$ | 1D | Aerosol backscatter coefficient at 532 nm retrieved with Raman method           |
|  |  | aerBsc_RR_1064    | $\text{sr}^{-1} \text{m}^{-1}$ | 1D | Aerosol backscatter coefficient at 1064 nm retrieved with rotation Raman method |
|  |  | aerBsc_RR_355     | $\text{sr}^{-1} \text{m}^{-1}$ | 1D | Aerosol backscatter coefficient at 355 nm retrieved with rotation Raman method  |
|  |  | aerBsc_RR_532     | $\text{sr}^{-1} \text{m}^{-1}$ | 1D | Aerosol backscatter coefficient at 532 nm retrieved with rotation               |



# L2A+

Ref: Ref: ESA AO/1-11041/22/I-NS

DI05: Output Data Product (OP)

Page: 10

|  |  |                   |                 |    |  |
|--|--|-------------------|-----------------|----|--|
|  |  |                   |                 |    | Raman method   |
|  |  | aerExt_raman_1064 | m <sup>-1</sup> | 1D | Aerosol extinction coefficient at 1064 nm retrieved with Raman method          |
|  |  | aerExt_raman_355  | m <sup>-1</sup> | 1D | Aerosol extinction coefficient at 355 nm retrieved with Raman method           |
|  |  | aerExt_raman_532  | m <sup>-1</sup> | 1D | Aerosol extinction coefficient at 532 nm retrieved with Raman method           |
|  |  | aerExt_RR_1064    | m <sup>-1</sup> | 1D | Aerosol extinction coefficient at 1064 nm retrieved with rotation Raman method |
|  |  | aerExt_RR_355     | m <sup>-1</sup> | 1D | Aerosol extinction coefficient at 355 nm retrieved with rotation Raman method  |
|  |  | aerExt_RR_532     | m <sup>-1</sup> | 1D | Aerosol extinction coefficient at 532 nm retrieved with rotation Raman method  |
|  |  | aerLR_raman_1064  | sr              | 1D | Aerosol lidar ratio at 1064 nm retrieved with Raman method                     |



|  |                 |                                       |    |   |
|--|-----------------|---------------------------------------|----|---|
|  | aerLR_raman_355 | sr                                    | 1D | Aerosol lidar ratio at 355 nm retrieved with Raman method           |
|  | aerLR_raman_532 | sr                                    | 1D | Aerosol lidar ratio at 532 nm retrieved with Raman method           |
|  | aerLR_RR_1064   | sr                                    | 1D | Aerosol lidar ratio at 1064 nm retrieved with rotation Raman method |
|  | aerLR_RR_355    | sr                                    | 1D | Aerosol lidar ratio at 355 nm retrieved with rotation Raman method  |
|  | aerLR_RR_532    | sr                                    | 1D | Aerosol lidar ratio at 532 nm retrieved with rotation Raman method  |
|  | altitude        | m                                     | -  | Height of lidar above mean sea level                                |
|  | end_time        | seconds since 1970-01-01 00:00:00 UTC | -  | Time UTC of the end of the current measurement                      |
|  | height          | m                                     | 1D | Height above ground   |
|  | latitude        | degrees north                         | -  | Latitude of the site  |
|  | longitude       | degrees east                          | -  | Longitude of the site   |
|  | LR_aeronet_1064 | sr                                    | -  | Aerosol lidar ratio at 1064 nm retrieved                            |



|  |  |                     |    |    |  |
|--|--|---------------------|----|----|--|
|  |  |                     |    |    | with constrained-AOD method  |
|  |  | LR_aeronet_355      | sr | -  | Aerosol lidar ratio at 355 nm retrieved with constrained-AOD method    |
|  |  | LR_aeronet_532      | sr | -  | Aerosol lidar ratio at 532 nm retrieved with constrained-AOD method    |
|  |  | parDepol_klett_1064 | -  | 1D | Particle linear depolarization ratio at 1064 nm with Klett backscatter |
|  |  | parDepol_klett_355  | -  | 1D | Particle linear depolarization ratio at 355 nm with Klett backscatter  |
|  |  | parDepol_klett_532  | -  | 1D | Particle linear depolarization ratio at 532 nm with Klett backscatter  |
|  |  | parDepol_raman_1064 | -  | 1D | Particle linear depolarization ratio at 1064 nm with Raman backscatter |
|  |  | parDepol_raman_355  | -  | 1D | Particle linear depolarization ratio at 355 nm with                    |



|  |  |                                 |                                       |                   |   |
|--|--|---------------------------------|---------------------------------------|-------------------|---|
|  |  |                                 |                                       | Raman backscatter |   |
|  |  | parDepol_raman_532              | -                                     | 1D                | Particle linear depolarization ratio at 532 nm with Raman backscatter |
|  |  | pressure                        | hPa                                   | 1D                | Air pressure  |
|  |  | reference_height_1064           | m                                     | 1D                | Reference height for 1064 nm  |
|  |  | reference_height_355            | m                                     | 1D                | Reference height for 355 nm   |
|  |  | reference_height_532            | m                                     | 1D                | Reference height for 532 nm   |
|  |  | RH                              | %                                     | 1D                | Relative humidity   |
|  |  | shots                           | -                                     | -                 | Accumulated laser shots   |
|  |  | start_time                      | seconds since 1970-01-01 00:00:00 UTC | -                 | Time UTC of the start of the current measurement                      |
|  |  | temperature                     | degree Celsius                        | 1D                | Air temperature   |
|  |  | uncertainty_aerBsc_aeronet_1064 | sr <sup>-1</sup> m <sup>-1</sup>      | 1D                | Uncertainty of aerosol backscatter coefficient at 1064 nm             |
|  |  | uncertainty_aerBsc_aeronet_355  | sr <sup>-1</sup> m <sup>-1</sup>      | 1D                | Uncertainty of aerosol backscatter coefficient at 355 nm              |
|  |  | uncertainty_aerBsc_aeronet_532  | sr <sup>-1</sup> m <sup>-1</sup>      | 1D                | Uncertainty of aerosol backscatter coefficient at 532 nm              |
|  |  | uncertainty_aerBsc_klett_1064   | sr <sup>-1</sup> m <sup>-1</sup>      | 1D                | Uncertainty of aerosol  |



|  |  |                               |                                  |    |   |
|--|--|-------------------------------|----------------------------------|----|---|
|  |  |                               |                                  |    | backscatter coefficient at 1064 nm                        |
|  |  | uncertainty_aerBsc_klett_355  | sr <sup>-1</sup> m <sup>-1</sup> | 1D | Uncertainty of aerosol backscatter coefficient at 355 nm  |
|  |  | uncertainty_aerBsc_klett_532  | sr <sup>-1</sup> m <sup>-1</sup> | 1D | Uncertainty of aerosol backscatter coefficient at 532 nm  |
|  |  | uncertainty_aerBsc_raman_1064 | sr <sup>-1</sup> m <sup>-1</sup> | 1D | Uncertainty of aerosol backscatter coefficient at 1064 nm |
|  |  | uncertainty_aerBsc_raman_355  | sr <sup>-1</sup> m <sup>-1</sup> | 1D | Uncertainty of aerosol backscatter coefficient at 355 nm  |
|  |  | uncertainty_aerBsc_raman_532  | sr <sup>-1</sup> m <sup>-1</sup> | 1D | Uncertainty of aerosol backscatter coefficient at 532 nm  |
|  |  | uncertainty_aerBsc_RR_1064    | sr <sup>-1</sup> m <sup>-1</sup> | 1D | Uncertainty of aerosol backscatter coefficient at 1064 nm |
|  |  | uncertainty_aerBsc_RR_355     | sr <sup>-1</sup> m <sup>-1</sup> | 1D | Uncertainty of aerosol backscatter coefficient at 355 nm  |
|  |  | uncertainty_aerBsc_RR_532     | sr <sup>-1</sup> m <sup>-1</sup> | 1D | Uncertainty of aerosol backscatter coefficient at 532 nm  |
|  |  | uncertainty_aerExt_raman_1064 | m <sup>-1</sup>                  | 1D | Uncertainty of aerosol extinction coefficient at 1064 nm  |
|  |  | uncertainty_aerExt_raman_355  | m <sup>-1</sup>                  | 1D | Uncertainty of aerosol extinction                         |



# L2A+

Ref: *ESA AO/1-11041/22/I-NS*

DI05: Output Data Product (OP)

Page: 15

|  |  |                                 |                 |    |  |
|--|--|---------------------------------|-----------------|----|--|
|  |  |                                 |                 |    | coefficient at 355 nm  |
|  |  | uncertainty_aerExt_raman_532    | m <sup>-1</sup> | 1D | Uncertainty of aerosol extinction coefficient at 532 nm        |
|  |  | uncertainty_aerExt_RR_1064      | m <sup>-1</sup> | 1D | Uncertainty of aerosol extinction coefficient at 1064 nm       |
|  |  | uncertainty_aerExt_RR_355       | m <sup>-1</sup> | 1D | Uncertainty of aerosol extinction coefficient at 355 nm        |
|  |  | uncertainty_aerExt_RR_532       | m <sup>-1</sup> | 1D | Uncertainty of aerosol extinction coefficient at 532 nm        |
|  |  | uncertainty_aerLR_raman_1064    | m <sup>-1</sup> | 1D | Uncertainty of aerosol lidar ratio at 1064 nm                  |
|  |  | uncertainty_aerLR_raman_355     | sr              | 1D | Uncertainty of aerosol lidar ratio at 355 nm                   |
|  |  | uncertainty_aerLR_raman_532     | sr              | 1D | Uncertainty of aerosol lidar ratio at 532 nm                   |
|  |  | uncertainty_aerLR_RR_1064       | sr              | 1D | Uncertainty of aerosol lidar ratio at 1064 nm                  |
|  |  | uncertainty_aerLR_RR_355        | sr              | 1D | Uncertainty of aerosol lidar ratio at 355 nm                   |
|  |  | uncertainty_aerLR_RR_532        | sr              | 1D | Uncertainty of aerosol lidar ratio at 532 nm                   |
|  |  | uncertainty_parDepol_klett_1064 | -               | 1D | Uncertainty of particle linear depolarization ratio at 1064 nm |



|  |  |                                 |   |    |   |
|--|--|---------------------------------|---|----|---|
|  |  |                                 |   |    | with Klett backscatter  |
|  |  | uncertainty_parDepol_klett_355  | - | 1D | Uncertainty of particle linear depolarization ratio at 355 nm with Klett backscatter  |
|  |  | uncertainty_parDepol_klett_532  | - | 1D | Uncertainty of particle linear depolarization ratio at 532 nm with Klett backscatter  |
|  |  | uncertainty_parDepol_raman_1064 | - | 1D | Uncertainty of particle linear depolarization ratio at 1064 nm with Raman backscatter |
|  |  | uncertainty_parDepol_raman_355  | - | 1D | Uncertainty of particle linear depolarization ratio at 355 nm with Raman backscatter  |
|  |  | uncertainty_parDepol_raman_532  | - | 1D | Uncertainty of particle linear depolarization ratio at 532 nm with Raman backscatter  |
|  |  | uncertainty_volDepol_klett_1064 | - | 1D | Uncertainty of volume depolarization ratio at 1064 nm                                 |
|  |  | uncertainty_volDepol_klett_355  | - | 1D | Uncertainty of volume depolarization ratio at 355 nm                                  |



|  |  |                                 |      |    |   |
|--|--|---------------------------------|------|----|---|
|  |  | uncertainty_volDepol_klett_532  | -    | 1D | Uncertainty of volume depolarization ratio at 532 nm                                  |
|  |  | uncertainty_volDepol_raman_1064 | -    | 1D | Uncertainty of volume depolarization ratio at 1064 nm                                 |
|  |  | uncertainty_volDepol_raman_355  | -    | 1D | Uncertainty of volume depolarization ratio at 355 nm                                  |
|  |  | uncertainty_volDepol_raman_532  | -    | 1D | Uncertainty of volume depolarization ratio at 532 nm                                  |
|  |  | uncertainty_WVMR                | g/km | 1D | Absolute water vapor mixing ratio uncertainty   |
|  |  | volDepol_klett_1064             | -    | 1D | Volume linear depolarization ratio at 1064 nm with the same smoothing as Klett method |
|  |  | volDepol_klett_355              | -    | 1D | Volume linear depolarization ratio at 355 nm with the same smoothing as Klett method  |
|  |  | volDepol_klett_532              | -    | 1D | Volume linear depolarization ratio at 532 nm with the same smoothing as Klett method  |



|  |  |                     |        |    |   |
|--|--|---------------------|--------|----|---|
|  |  | volDepol_raman_1064 | -      | 1D | Volume linear depolarization ratio at 1064 nm with the same smoothing as Raman method |
|  |  | volDepol_raman_355  | -      | 1D | Volume linear depolarization ratio at 355 nm with the same smoothing as Raman method  |
|  |  | volDepol_raman_532  | -      | 1D | Volume linear depolarization ratio at 532 nm with the same smoothing as Raman method  |
|  |  | WVMR                | g/kg   | 1D | Water vapor mixing ratio  |
|  |  | WVMR_no_QC          | g/kg   | 1D | Water vapor mixing ratio without quality control                                      |
|  |  | WVMR_rel_err        | -      | 1D | Relative error of the water vapor mixing ratio  |
|  |  | zenith_angle        | degree | -  | Zenith angle  |



| Name  | Long Name  | Type       |
|---|--|------------|
| 2021_09_01_Wed_CPV_00_01_01_0001_0100_profiles.nc | 2021_09_01_Wed_CPV_00_01_01_0001_0100_profiles.nc                          | Local File |
| aerBsc_aeronet_1064                               | aerosol backscatter coefficient at 1064 nm retrieved with constrained-...  | 1D         |
| aerBsc_aeronet_355                                | aerosol backscatter coefficient at 355 nm retrieved with constrained-A...  | 1D         |
| aerBsc_aeronet_532                                | aerosol backscatter coefficient at 532 nm retrieved with constrained-A...  | 1D         |
| aerBsc_klett_1064                                 | aerosol backscatter coefficient at 1064 nm retrieved with Klett method     | 1D         |
| aerBsc_klett_355                                  | aerosol backscatter coefficient at 355 nm retrieved with Klett method      | 1D         |
| aerBsc_klett_532                                  | aerosol backscatter coefficient at 532 nm retrieved with Klett method      | 1D         |
| aerBsc_raman_1064                                 | aerosol backscatter coefficient at 1064 nm retrieved with Raman method     | 1D         |
| aerBsc_raman_355                                  | aerosol backscatter coefficient at 355 nm retrieved with Raman method      | 1D         |
| aerBsc_raman_532                                  | aerosol backscatter coefficient at 532 nm retrieved with Raman method      | 1D         |
| aerBsc_RR_1064                                    | aerosol backscatter coefficient at 1064 nm retrieved with rotation Rama... | 1D         |
| aerBsc_RR_355                                     | aerosol backscatter coefficient at 355 nm retrieved with rotation Rama...  | 1D         |
| aerBsc_RR_532                                     | aerosol backscatter coefficient at 532 nm retrieved with rotation Rama...  | 1D         |
| aerExt_raman_1064                                 | aerosol extinction coefficient at 1064 nm retrieved with Raman method      | 1D         |
| aerExt_raman_355                                  | aerosol extinction coefficient at 355 nm retrieved with Raman method       | 1D         |
| aerExt_raman_532                                  | aerosol extinction coefficient at 532 nm retrieved with Raman method       | 1D         |
| aerExt_RR_1064                                    | aerosol extinction coefficient at 1064 nm retrieved with rotation Rama...  | 1D         |
| aerExt_RR_355                                     | aerosol extinction coefficient at 355 nm retrieved with rotation Raman ... | 1D         |
| aerExt_RR_532                                     | aerosol extinction coefficient at 532 nm retrieved with rotation Raman ... | 1D         |
| aerLR_raman_1064                                  | aerosol lidar ratio at 1064 nm retrieved with Raman method                 | 1D         |
| aerLR_raman_355                                   | aerosol lidar ratio at 355 nm retrieved with Raman method                  | 1D         |
| aerLR_raman_532                                   | aerosol lidar ratio at 532 nm retrieved with Raman method                  | 1D         |
| aerLR_RR_1064                                     | aerosol lidar ratio at 1064 nm retrieved with rotation Raman method        | 1D         |
| aerLR_RR_355                                      | aerosol lidar ratio at 355 nm retrieved with rotation Raman method         | 1D         |
| aerLR_RR_532                                      | aerosol lidar ratio at 532 nm retrieved with rotation Raman method         | 1D         |
| altitude  | Height of lidar above mean sea level                                       | —          |
| end_time  | Time UTC to finish the current measurement                                 | —          |
| height  | Height above the ground  | 1D         |
| latitude  | Latitude of the site   | —          |
| longitude   | Longitude of the site  | —          |
| LR_aeronet_1064                                   | aerosol lidar ratio at 1064 nm retrieved with constrained-AOD method       | —          |
| LR_aeronet_355                                    | aerosol lidar ratio at 355 nm retrieved with constrained-AOD method        | —          |
| LR_aeronet_532                                    | aerosol lidar ratio at 532 nm retrieved with constrained-AOD method        | —          |
| parDepol_klett_1064                               | particle linear depolarization ratio at 1064 nm with Klett backscatter     | 1D         |
| parDepol_klett_355                                | particle linear depolarization ratio at 355 nm with Klett backscatter      | 1D         |
| parDepol_klett_532                                | particle linear depolarization ratio at 532 nm with Klett backscatter      | 1D         |
| parDepol_raman_1064                               | particle linear depolarization ratio at 1064 nm with Raman backscatter     | 1D         |
| parDepol_raman_355                                | particle linear depolarization ratio at 355 nm with Raman backscatter      | 1D         |
| parDepol_raman_532                                | particle linear depolarization ratio at 532 nm with Raman backscatter      | 1D         |
| pressure  | pressure   | 1D         |
| reference_height_1064                             | reference height for 1064 nm   | 1D         |
| reference_height_355                              | reference height for 355 nm  | 1D         |
| reference_height_532                              | reference height for 532 nm  | 1D         |
| RH  | relative humidity  | 1D         |
| shots   | accumulated laser shots  | —          |
| start_time  | Time UTC to start the current measurement                                  | —          |
| temperature                                       | temperature  | 1D         |
| uncertainty_aerBsc_aeronet_1064                   | uncertainty of aerosol backscatter coefficient at 1064 nm                  | 1D         |
| uncertainty_aerBsc_aeronet_355                    | uncertainty of aerosol backscatter coefficient at 355 nm                   | 1D         |
| uncertainty_aerBsc_aeronet_532                    | uncertainty of aerosol backscatter coefficient at 532 nm                   | 1D         |
| uncertainty_aerBsc_klett_1064                     | uncertainty of aerosol backscatter coefficient at 1064 nm                  | 1D         |
| uncertainty_aerBsc_klett_355                      | uncertainty of aerosol backscatter coefficient at 355 nm                   | 1D         |
| uncertainty_aerBsc_klett_532                      | uncertainty of aerosol backscatter coefficient at 532 nm                   | 1D         |
| uncertainty_aerBsc_raman_1064                     | uncertainty of aerosol backscatter coefficient at 1064 nm                  | 1D         |
| uncertainty_aerBsc_raman_355                      | uncertainty of aerosol backscatter coefficient at 355 nm                   | 1D         |
| uncertainty_aerBsc_raman_532                      | uncertainty of aerosol backscatter coefficient at 532 nm                   | 1D         |
| uncertainty_aerBsc_RR_1064                        | uncertainty of aerosol backscatter coefficient at 1064 nm                  | 1D         |
| uncertainty_aerBsc_RR_355                         | uncertainty of aerosol backscatter coefficient at 355 nm                   | 1D         |
| uncertainty_aerBsc_RR_532                         | uncertainty of aerosol backscatter coefficient at 532 nm                   | 1D         |
| uncertainty_aerExt_raman_1064                     | uncertainty of aerosol extinction coefficient at 1064 nm                   | 1D         |



# L2A+

Ref: *ESA AO/1-11041/22/I-NS*

DI05: Output Data Product (OP)

Page: 20

|                                 |   |    |
|---------------------------------|---|----|
| uncertainty_aerExt_raman_355    | uncertainty of aerosol extinction coefficient at 355 nm                       | 1D |
| uncertainty_aerExt_raman_532    | uncertainty of aerosol extinction coefficient at 532 nm                       | 1D |
| uncertainty_aerExt_RR_1064      | uncertainty of aerosol extinction coefficient at 1064 nm                      | 1D |
| uncertainty_aerExt_RR_355       | uncertainty of aerosol extinction coefficient at 355 nm                       | 1D |
| uncertainty_aerExt_RR_532       | uncertainty of aerosol extinction coefficient at 532 nm                       | 1D |
| uncertainty_aerLR_raman_1064    | uncertainty of aerosol lidar ratio at 1064 nm                                 | 1D |
| uncertainty_aerLR_raman_355     | uncertainty of aerosol lidar ratio at 355 nm                                  | 1D |
| uncertainty_aerLR_raman_532     | uncertainty of aerosol lidar ratio at 532 nm                                  | 1D |
| uncertainty_aerLR_RR_1064       | uncertainty of aerosol lidar ratio at 1064 nm                                 | 1D |
| uncertainty_aerLR_RR_355        | uncertainty of aerosol lidar ratio at 355 nm                                  | 1D |
| uncertainty_aerLR_RR_532        | uncertainty of aerosol lidar ratio at 532 nm                                  | 1D |
| uncertainty_parDepol_klett_1064 | uncertainty of particle linear depolarization ratio at 1064 nm with Klett ... | 1D |
| uncertainty_parDepol_klett_355  | uncertainty of particle linear depolarization ratio at 355 nm with Klett b... | 1D |
| uncertainty_parDepol_klett_532  | uncertainty of particle linear depolarization ratio at 532 nm with Klett b... | 1D |
| uncertainty_parDepol_raman_1064 | uncertainty of particle linear depolarization ratio at 1064 nm with Rama...   | 1D |
| uncertainty_parDepol_raman_355  | uncertainty of particle linear depolarization ratio at 355 nm with Raman...   | 1D |
| uncertainty_parDepol_raman_532  | uncertainty of particle linear depolarization ratio at 532 nm with Raman...   | 1D |
| uncertainty_volDepol_klett_1064 | uncertainty of volume depolarization ratio at 1064 nm                         | 1D |
| uncertainty_volDepol_klett_355  | uncertainty of volume depolarization ratio at 355 nm                          | 1D |
| uncertainty_volDepol_klett_532  | uncertainty of volume depolarization ratio at 532 nm                          | 1D |
| uncertainty_volDepol_raman_1064 | uncertainty of volume depolarization ratio at 1064 nm                         | 1D |
| uncertainty_volDepol_raman_355  | uncertainty of volume depolarization ratio at 355 nm                          | 1D |
| uncertainty_volDepol_raman_532  | uncertainty of volume depolarization ratio at 532 nm                          | 1D |
| uncertainty_WVMR                | absolute water vapor mixing ratio uncertainty                                 | 1D |
| volDepol_klett_1064             | volume linear depolarization ratio at 1064 nm with the same smoothing ...     | 1D |
| volDepol_klett_355              | volume linear depolarization ratio at 355 nm with the same smoothing a...     | 1D |
| volDepol_klett_532              | volume linear depolarization ratio at 532 nm with the same smoothing a...     | 1D |
| volDepol_raman_1064             | volume linear depolarization ratio at 1064 nm with the same smoothing ...     | 1D |
| volDepol_raman_355              | volume linear depolarization ratio at 355 nm with the same smoothing a...     | 1D |
| volDepol_raman_532              | volume linear depolarization ratio at 532 nm with the same smoothing a...     | 1D |
| WVMR                            | water vapor mixing ratio  | 1D |
| WVMR_no_QC                      | water vapor mixing ratio without Quality control                              | 1D |
| WVMR_rel_error                  | relative error of the water vapor mixing ratio                                | 1D |
| zenith_angle                    | laser pointing angle with respect to the zenith                               | —  |

Figure 3: Indicative file output of PollyXT optical properties.

### 2.3. Access Credentials

Access to the ESA-L2A+ products are provided according to the following access credentials:

Table 3: ESA L2A+ WP2000 access credentials.

|           |                    |
|-----------|--------------------|
| WP2000    |                    |
| Protocol: | SFTP (Port 22)     |
| Username: | l2aplus_wp2000     |
| Password: | eYst5kuxngzn       |
| Host:     | react.space.noa.gr |

### 2.4. Contact Person.

#### Contact:

Users can contact with Athina Floutsi (floutsi@tropos.de) or/and Holger Baars (baars@tropos.de) for any further details and clarifications regarding the L2A+ dataset outputs of L2A+ WP2000.



# L2A+

## 3. The L2A+ Product.

### 3.1. Introduction.

This section provides an overview of the novel L2A+ aerosol product established on the basis of Aeolus. More specifically, the product is derived on the basis of a synergistic approach involving spaceborne retrievals from multi-sensors in conjunction with reanalysis numerical outputs and reference ground-based measurements. The period of interest includes the months of July, September of 2021 and June, September of 2022 which coincides with the Joint Aeolus Tropical Atlantic Campaign (JATAC), on the islands of Cabo Verde during the ASKOS experiment. Information on the development is provided in the framework of the ESA L2A+ DI03 entitled “Description of the Algorithm Developments (ALGO)”. The present section provides an overview of the L2A+ products in terms of filename format (Sect.3.2), the L2A+ output products for an indicative Aeolus study case (Sect.3.3), the basic products included in the output NetCDF file (Sect.3.4), access credentials (Sect.3.5), and contact person information (Sect.3.6)

### 3.2. Filename Format

L2A+ filename: “AE\_OPER\_ALD\_U\_N\_2A\_DD MMM\_YYYY\_hh\_mm\_ss\_hh\_mm\_ss.nc”

Table 4: L2A+ filename descriptor.

| Filename Descriptor |   | Explanation  |
|---------------------|---|--|
| AE                  | ⇒ | Aeolus mission   |
| OPER                | ⇒ | File class: Routine operations                           |
| ALD                 | ⇒ | Data product from the Aladin instrument                  |
| U                   | ⇒ | Unconsolidated   |
| N                   | ⇒ | Nominal instrument operation                             |
| 2A                  | ⇒ | Product ID: Level 2A product                             |
| yyyymmddThhmmsszzz  | ⇒ | start time of sensing (date/time string: precision 1 ms) |
| ‘uuuuuuuuu’         | ⇒ | duration/sensing period                                  |
| ‘oooooo’            | ⇒ | start absolute orbit number                              |
| ‘vvvv’              | ⇒ | file version number                                      |

### 3.3. Indicative Study-Case: The Aeolus-Cabo Verde overpass on the 10th of September 2021

#### 3.3.1. Description of the atmospheric scene.

Figure 4a illustrates the L2A+ region of interest with the blue-colored line indicating the ascending ALADIN’s measurement track for the given case. Next, Figure 4b illustrates for the specific study case, the time-closest binary cloud mask (CMa) product retrieved from the SEVIRI CLAAS-3 cloud dataset which as we can see in the figure, describes the scene type (either 'clear' or 'cloudy') on a pixel level. The Aeolus’s ascending orbit is also depicted on the same figure with the red-coloured line. Based on the specific cloud-filtering procedure, the Aeolus SCA, SCA mid-bin and MLE backscatter retrievals, throughout the probed atmosphere by ALADIN, have been excluded from the analysis when the cloud fraction in each BRC profile exceeds a given threshold value (60% in this case).



# L2A+

Ref: *ESA AO/1-11041/22/I-NS*

DI05: Output Data Product (OP)

Page: 22

## Aeolus Orbit

## MSG Cloud Coverage

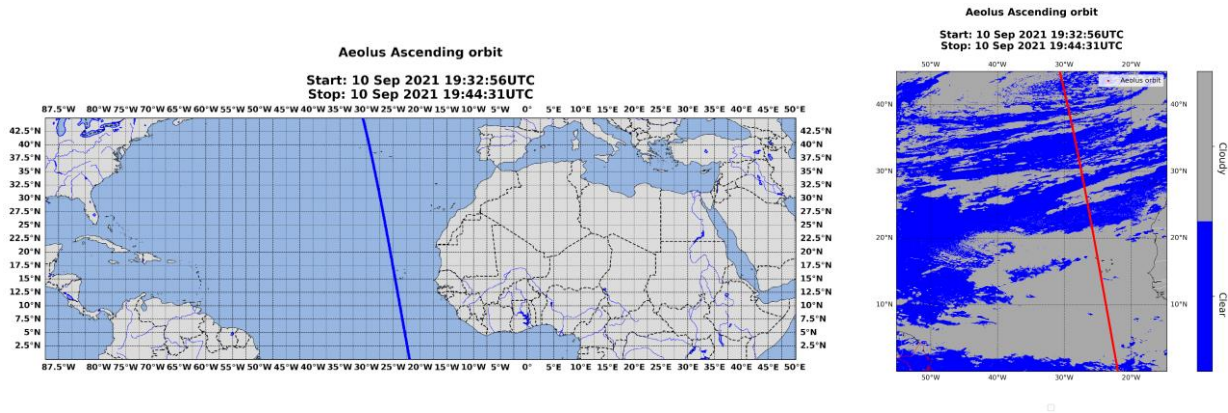
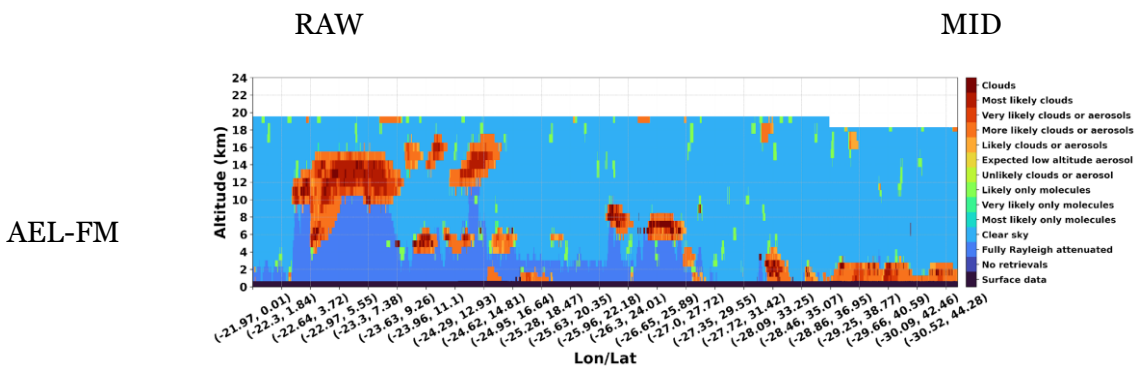


Figure 4: a) Aeolus ascending orbit (id: 017679) over the L2A+ RoI on 10<sup>th</sup> September 2021 and b) the time-closest spatial distribution of clouds derived from the binary cloud-mask product of MSG-SEVIRI CLAAS-3 dataset.

In Figure 5a, the retrieved AEL-FM feature-mask product along the given Aeolus’s measurement track is presented where we can observe the classified features of the probed atmospheric scene. It can be seen that the features associated with “strong” returns mainly attributed to clouds or high optically thick aerosol layers are colorized in brown and orange respectively while those associated with the molecular atmosphere or clear sky conditions are colorized in green and cyan respectively. According to the figure, one can clearly distinguish a large number of strong features that have been classified as (likely and most likely) clouds (FM values of 6 to 10) along the largest part of the given Aeolus’s measurement track and especially between latitudes of 0 and 7° N and altitudes between 4 and 14 km above the ground. Following our filtering methodology, these features can be detected and excluded from the analysis in order to acquire the pure aerosol profiles. In the two figures below, the transformed feature mask product to the Aeolus’s horizontal and vertical resolution is provided separately for the regular Aeolus’s vertical scale (24 vertical bins) (Figure 5b) and middle-bin (23 vertical bins) scale (Figure 5c) with each bin expressing the cloud fraction (in %) of the specific BRC bin after computing the total percentage of cloud-contaminated measurements for the specific bin. Based on the transformed feature mask product, all Aeolus’s BRC bins with cloud fraction exceeding 0% were excluded from the analysis with the corresponding bins of the SCA, SCA mid-bin and MLE backscatter profiles.





FM

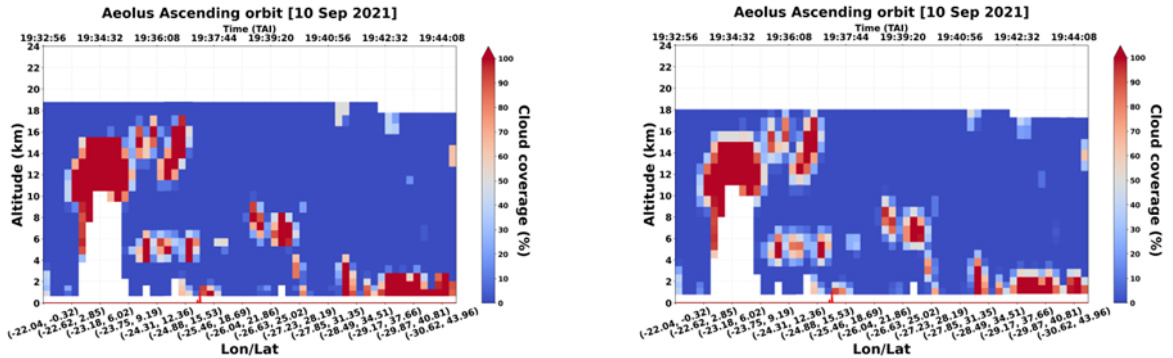


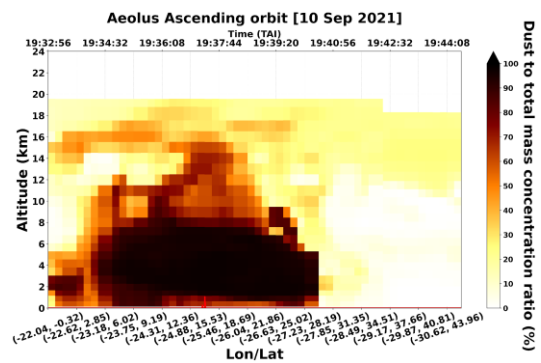
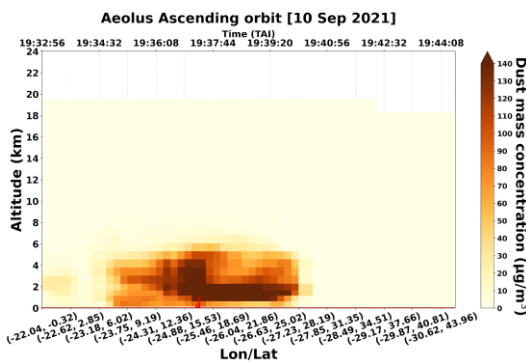
Figure 5: a) AEL-FM feature mask product along the Aeolus orbit (id: 017679) on 10<sup>th</sup> September 2021 and the transformed feature mask product on the Aeolus vertical and horizontal resolution for the b) regular (24 bins) and c) middle-bin scale (23 bins).

In the figure below, we present the horizontally integrated and vertically resolved Aeolus-like dust mass concentration profiles from CAMS along the Aeolus orbit (id: 017679), provided separately for the regular (Figure 6a) and middle-bin (Figure 6c) Aeolus' vertical scales (24, and 23 vertical bins respectively). According to the figure, a dust layer is identified over the latitudinal band of 5°- 25°N and up to 6km with elevated dust mass concentration values exceeding in many cases the value of 50  $\mu\text{g}/\text{m}^3$ . Additionally, for both vertical scales, the vertical profiles of the dust-to-total mass concentration ratio values (in percentage) along the Aeolus measurement track are also depicted in Figures 6b, and d. Based on both parameters retrieved from CAMS, the pure dust profiles were derived after eliminating all the BRC bins with dust concentration below 1.3  $\mu\text{g}/\text{m}^3$  (median value) and dust-to-total ratio below 50%.

Dust Mass Concentration  
( $\mu\text{g}/\text{m}^3$ )

Dust Percentage  
(%)

R  
A  
W



M  
I  
D

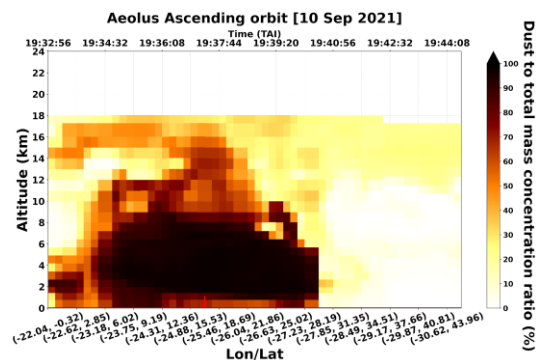
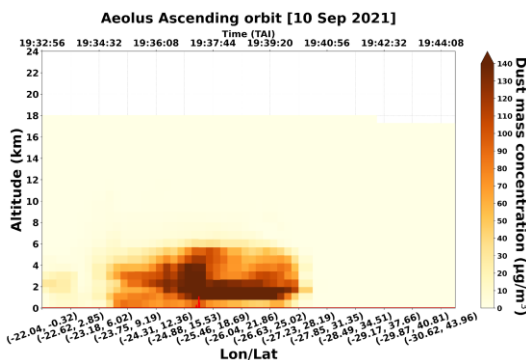




Figure 6: Vertical profiles of CAMS dust mass concentration and dust-to-total aerosol mass concentration ratio along the Aeolus orbit (id: 017679) provided in the regular (a, b) and middle-bin (c, d) vertical scales on the 10th of September 2021.

For the specific study case, the time-closest vertical profiles of CALIPSO total backscatter coefficient at 532 nm (Figure 7a), particulate depolarization ratio at 532 nm (Figure 7b) and the quality-assured (QA) pure-aerosol (Figure 7c) and pure-dust backscatter coefficient (Figure 7d) are also illustrated.

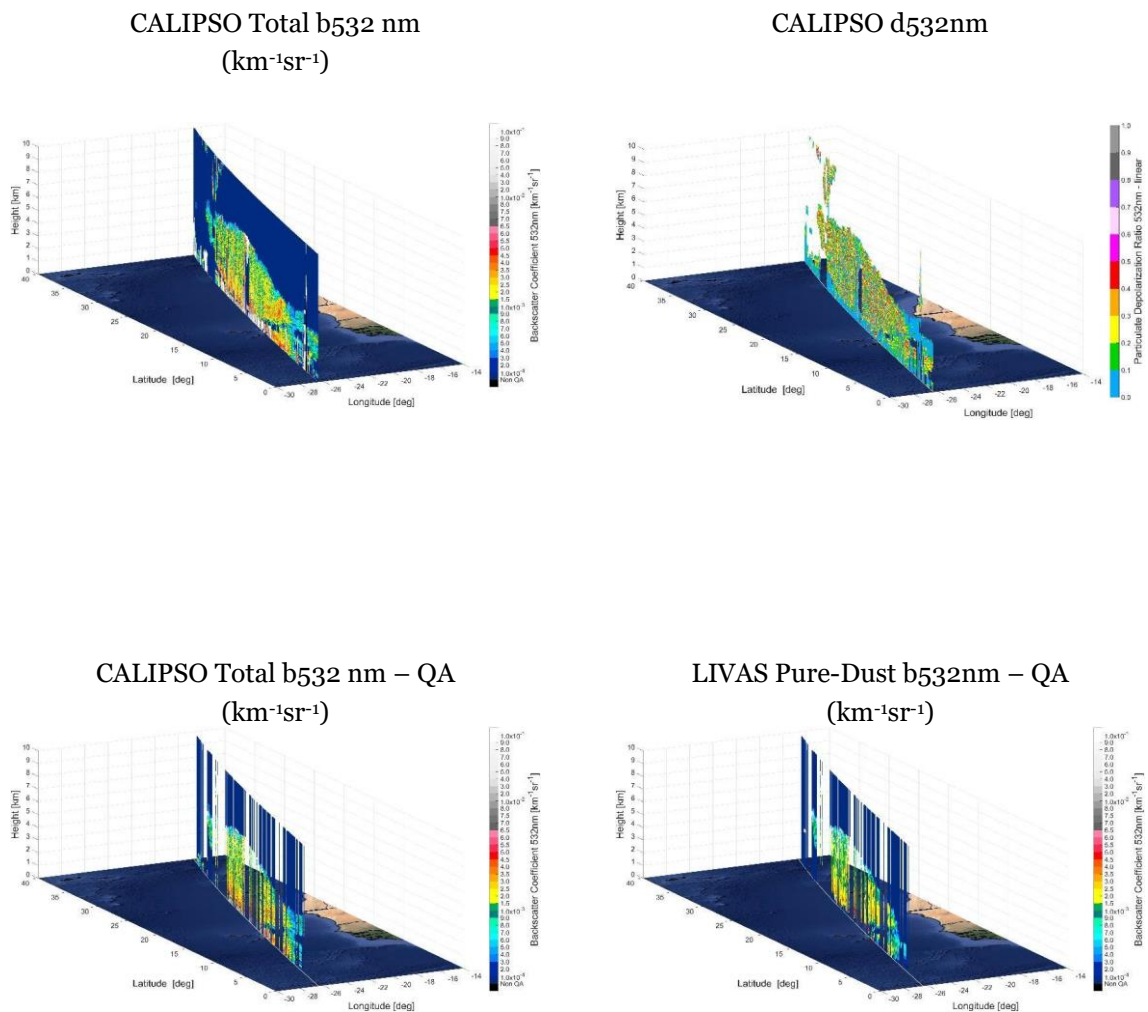


Figure 7: (a) CALIPSO total backscatter coefficient at 532 nm. (b) CALIPSO particulate depolarization ratio at 532 nm (c) CALIPSO QA pure-aerosol total backscatter coefficient at 532 nm (d) CALIPSO QA pure-dust backscatter coefficient at 532 nm.



### 3.3.2. Aeolus Optical Products.

In figure 8, the left panel illustrates the vertical profiles of the raw (unprocessed) Aeolus L2A retrievals of backscatter coefficient at 355 nm along the Aeolus overpass (id 017679), produced by the SCA, SCA mid-bin and MLE algorithms, while the right panel depicts the quality-assured (QA) backscatter profiles derived from the corresponding algorithms after implementing the cloud-filtering methodology using both the AEL-FM feature mask and MSG-SEVIRI Claas-3 cloud-mask retrievals. It has to be noted that the later ones correspond to the pure-aerosol backscatter profiles along the Aeolus overpass, since most of bins were rejected from the cloud-filtering process.

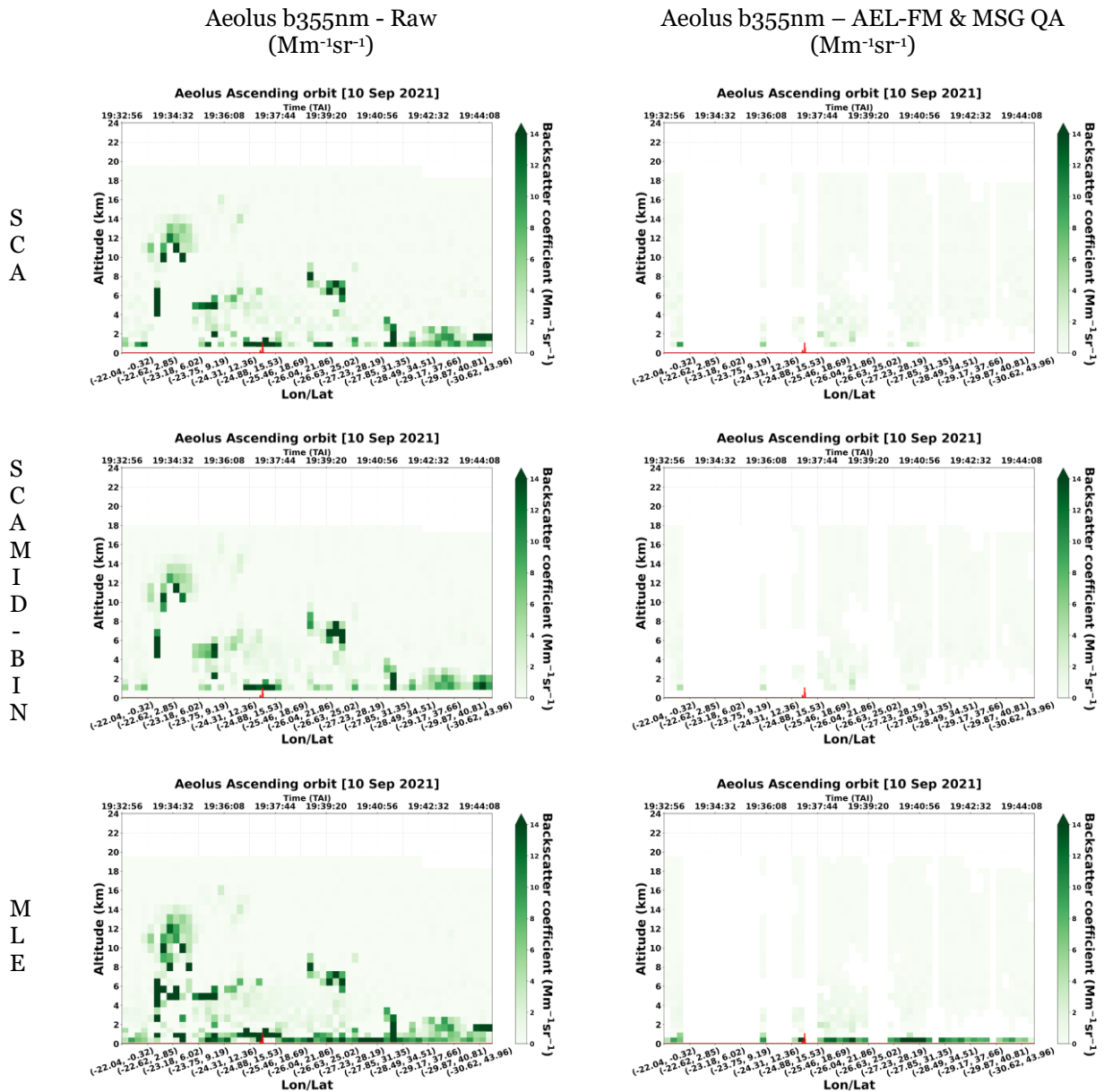


Figure 8: Raw Aeolus L2A backscatter profiles at 355 nm along the Aeolus orbit (id 017679) retrieved from the SCA, SCA mid-bin and MLE algorithms (left panel) and the corresponding QA pure-aerosol backscatter profiles at 355 nm for the SCA, SCA mid-bin and MLE algorithms (right panel).



# L2A+

### 3.3.3. L2A and L2A+ products.

Figure 9 gives for the given study case, an example of the pure-dust Aeolus co-polar backscatter profiles at 355 nm produced with the SCA and SCA mid-bin algorithms and the associated missing cross-polar backscatter component for each profile. Using both backscatter components (co + cross) the total (L2A+) backscatter profiles at 355 nm were derived and were used for the reconstruction of the pure-dust L2A extinction coefficient.

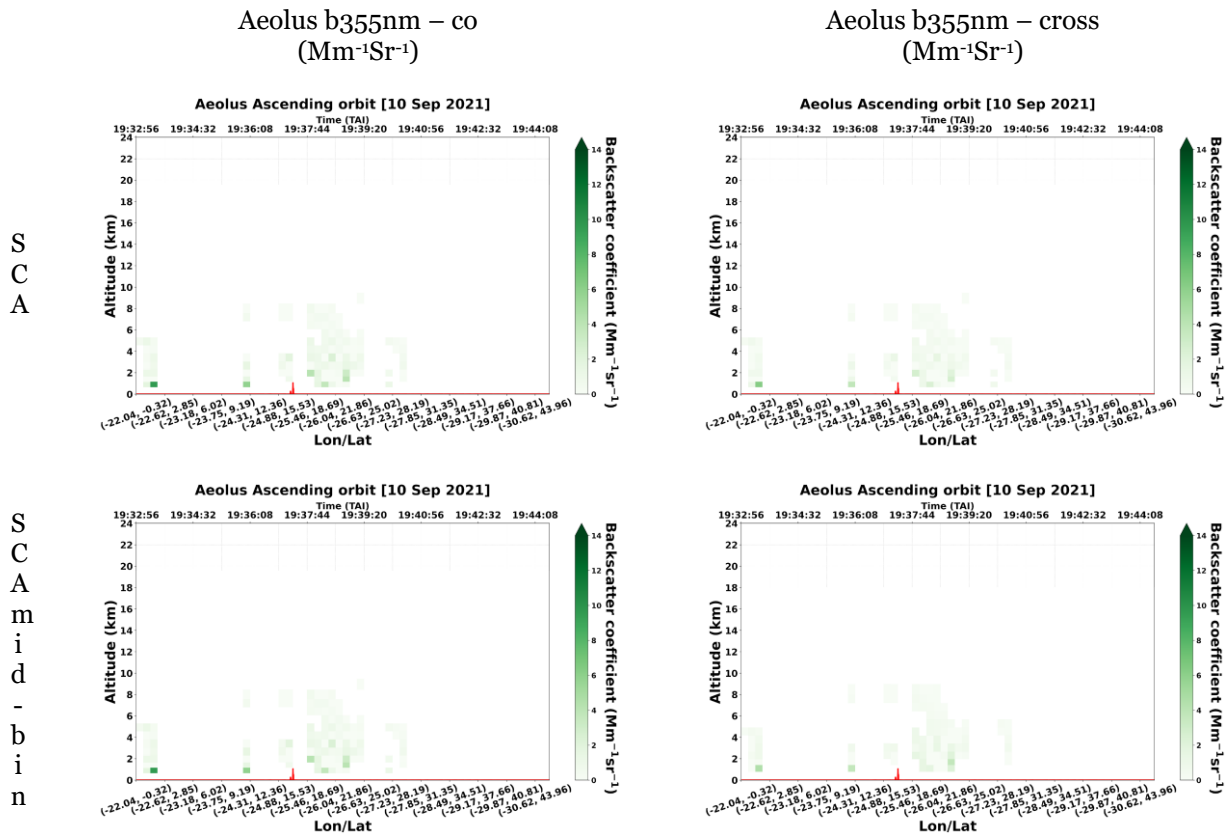


Figure 9: Co-polar and cross polar backscatter profiles along the Aeolus overpass (id 017679) for the SCA (a, b) and SCA mid-bin algorithms (c, d).

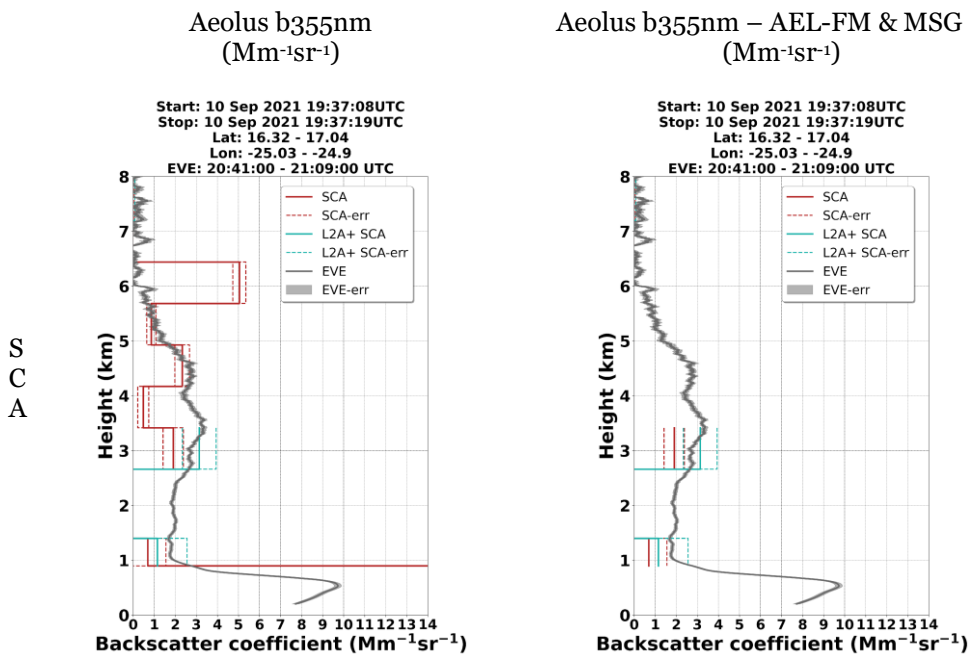
### 3.3.4. L2A+ - ESA-eVe validation.

The present section gives the intercomparison of Aeolus L2A and L2A+ aerosol optical products, in particular the backscatter coefficient at 355 nm retrieved with the SCA, SCA mid-bin and MLE algorithms against ground-based measurements from eVe lidar collected during the ASKOS experiment, under the Joint Aeolus Tropical Atlantic Campaign 2021 (JATAC), on the islands of Cabo Verde. The process was performed considering the raw (unprocessed) Aeolus L2A co-polar backscatter profiles at 355 nm for each of the aforementioned algorithms (SCA, SCA mid-bin, MLE) and the quality-assured (QA) pure-dust total (L2A+) backscatter profiles at 355 nm after the adjustment of the missing cross-polar component. It has to be noted that only the quality-assured (cloud-free) ground-based measurements were used for the comparison process. In the specific example, we present the intercomparison process which serves as a graphic example of the Aeolus performance for the first study case on 10<sup>th</sup> September 2021 presented in Figure 10.



According to our results, comparing the raw (left panel) and the QA Aeolus retrievals (right panel), it can be noticed that the implementation of the cloud-filtering and dust-typing methodologies for the derivation of the new Aeolus product (L2A+) produces a notable decrease in the amount of available data points since most of bins were rejected from the analysis. This can be noticed at around 6km where the large backscatter coefficients of the raw Aeolus L2A retrievals mostly attributed to cloud presence have been excluded in the QA retrievals. Moreover, looking at the raw Aeolus L2A retrievals, it can also be noticed a surface-related effect in the lowermost bins, retrieving an unreasonably large co-polar backscatter coefficient which was also rejected in the QA retrievals.

Next, focusing on the pure-dust layers of Aeolus L2A and L2A+ retrievals in Figure 10 (right panel), it can be noticed that after the correction of the backscattered signal, the L2A+ backscatter profiles present a better agreement with ground-based measurements than L2A retrievals. Especially, a fair agreement between the Aeolus L2A+ backscatter profile for the MLE algorithm and the corresponding ground-based system is pointed out throughout the vertical range of the detected dust layer.



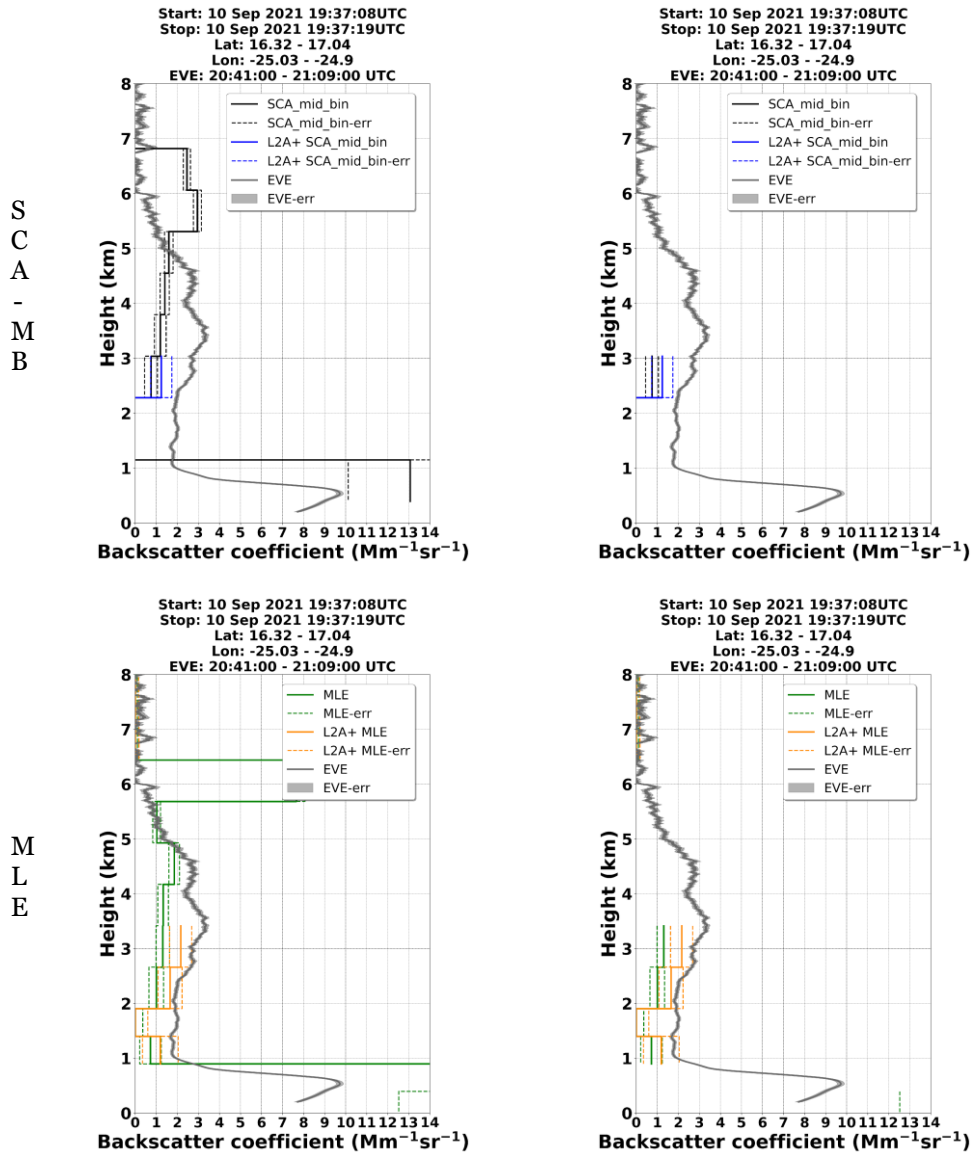


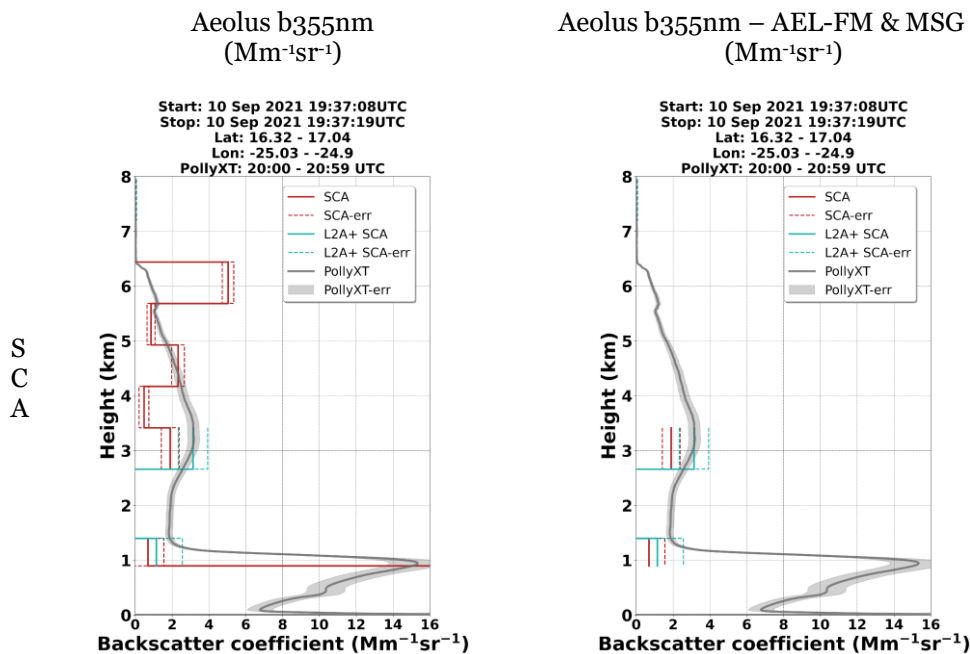
Figure 10: Vertical profiles of the raw Aeolus L2A and QA L2A+ backscatter coefficient at 355 nm retrieved from the SCA, SCA mid-bin and MLE algorithms with the corresponding backscatter profiles at 355 nm acquired by eVe ground-based lidar (left panel), and QA Aeolus L2A and L2A+ backscatter profiles for the SCA, SCA mid-bin and MLE algorithms with the derived backscatter profiles from eVe lidar (right panel).



# L2A+

### 3.3.5. L2A+ - ESA-PollyXT validation

The same intercomparison process was also performed between the vertically resolved Aeolus L2A/L2A+ backscatter coefficient at 355 nm for the SCA, SCA mid-bin and MLE algorithms and the corresponding time-nearest backscatter profiles at 532 nm from the PollyXT ground-based lidar operated at Mindelo station, Cabo Verde. The obtained results are presented in Figure 11 for the given study case on 10<sup>th</sup> September 2021. According to the results, we point out for the pure-dust layers (right panel), that for all the Aeolus L2A retrieval algorithms including the SCA, SCA mid-bin and MLE algorithms, the backscatter coefficient is underestimated throughout the whole vertical range of the detected dust layer. This difference is mostly attributed to the misdetection of the cross-polar component of the backscattered lidar signal when non-spherical mineral particles are recorded. Gkikas et al. (2023) also presented an underestimation that reached up to 33% in the aerosol backscatter coefficient after comparing the PollyXT and Aeolus-like PollyXT backscatter profiles for a study case on 10<sup>th</sup> July 2019 corroborating our findings. On the other hand, based on our results we can see that this difference is minimized and the satellite presents a satisfactory agreement with PollyXT lidar in the whole available profile when comparing the corrected L2A+ pure-dust total backscatter coefficient with the PollyXT-derived backscatter profile for all the available algorithms.



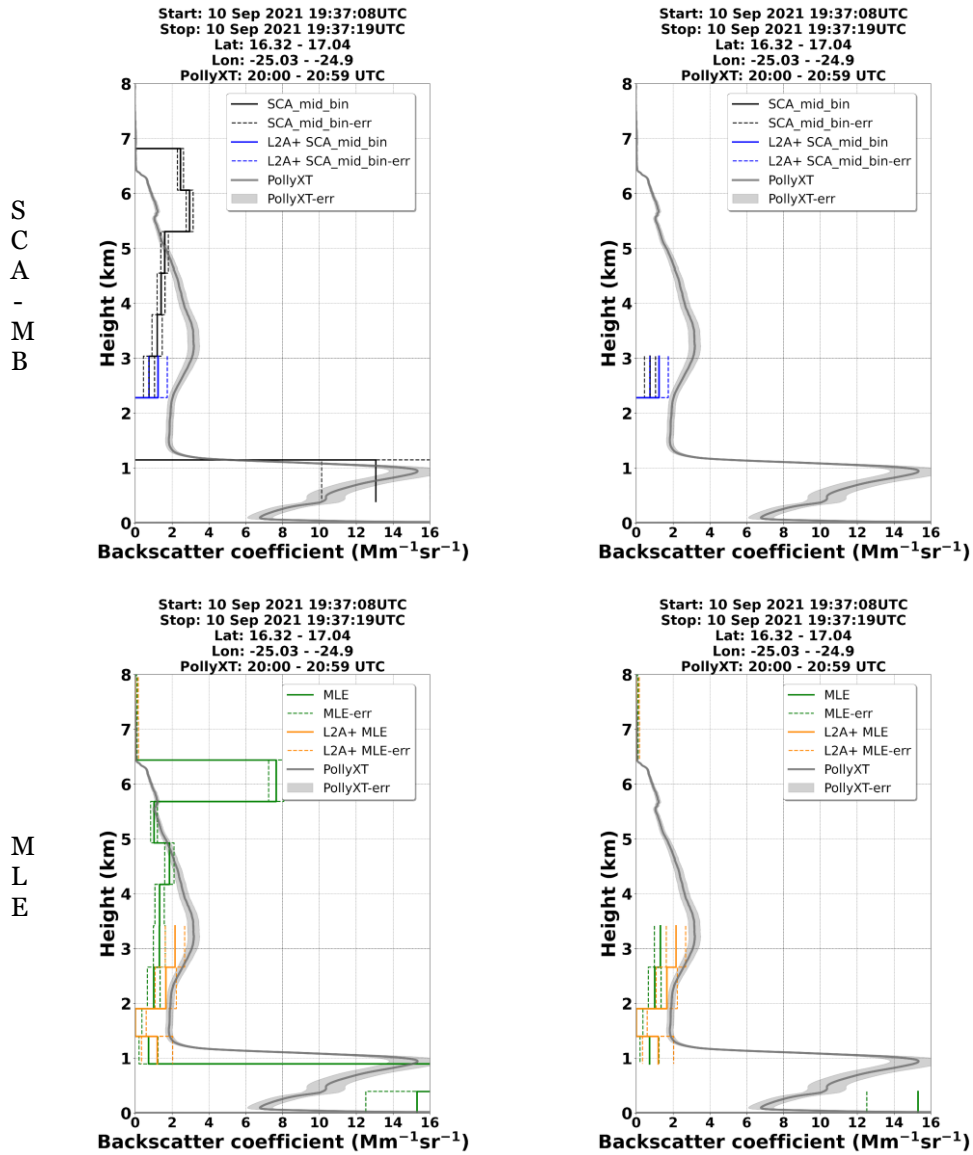
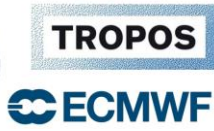


Figure 11: Vertical profiles of the raw Aeolus L2A and QA L2A+ backscatter coefficient at 355 nm retrieved from the SCA, SCA mid-bin and MLE algorithms with the corresponding backscatter profiles at 355 nm acquired by PollyXT ground-based lidar (left panel), and QA Aeolus L2A and L2A+ backscatter profiles for the SCA, SCA mid-bin and MLE algorithms with the derived backscatter profiles from PollyXT lidar (right panel).



# L2A+

## 3.4. The L2A+ products

This section provides an overview of the variables included in the L2A+ output files.

Table 5: Detailed description of the groups and variables of the final output L2A+ product.

| Group       | Subgroup         | Variable    | Units         | Dimensions             | Description  |
|-------------|------------------|-------------|---------------|------------------------|--|
| GEOLOCATION | DEM_INTERSECTION | measdem     | m             | 1d<br>(measurements)   | Altitude relative to the geoid of the intersection of the DEM and the line-of-sight. |
|             |                  | measdomlat  | degrees north | 1d<br>(measurements)   | Latitude of the intersection of the DEM and the line-of-sight.                       |
|             |                  | measdomlon  | degrees east  | 1d<br>(measurements)   | Longitude of the intersection of the DEM and the line-of-sight.                      |
|             |                  | measdomtime | Date format   | 1d<br>(measurements)   | Measurement centroid time from L1B.  |
|             | MIDDLE_BIN_SCALE | alt         | m             | 2d<br>(mb-lays, profs) | Bottom altitude of the middle bin.   |
|             |                  | lat         | degrees north | 2d<br>(mb-lays, profs) | Latitude of the start point of the profile middle bin.                               |
|             |                  | lon         | degrees east  | 2d<br>(mb-lays, profs) | Longitude of the start point of the profile middle bin.                              |
|             | REGULAR_SCALE    | alt         | m             | 2d<br>(lays, profs)    | Altitude of the lower edge of the height bin along the line-of-sight.                |
|             |                  | lat         | degrees north | 2d<br>(lays, profs)    | Latitude of the lower edge of the height bin   |



# L2A+

|            |  |                     |  |                     |  |
|------------|--|---------------------|--|---------------------|--|
|            |  |                     |  |                     | along the line-of-sight.   |
|            |  | lon                 | degrees east                             | 2d<br>(lays, profs) | Longitude of the lower edge of the height bin along the line-of-sight. |
| RAW DATA   | SCA                                      | alpha               | $10^{-6} \text{ m}^{-1}$                 | 2d<br>(lays, profs) | Particle extinction coefficient of the bin.                            |
|            |  | alpha_error         | $10^{-6} \text{ m}^{-1}$                 | 2d<br>(lays, profs) | Extinction error   |
|            |  |                     |  |                     |  |
|            |  | beta                | $10^{-6} \text{ sr}^{-1} \text{ m}^{-1}$ | 2d<br>(lays, profs) | Particle backscatter coefficient of the bin                            |
| beta_error | $10^{-6} \text{ sr}^{-1} \text{ m}^{-1}$ | 2d<br>(lays, profs) | Backscatter error                        |                     |  |



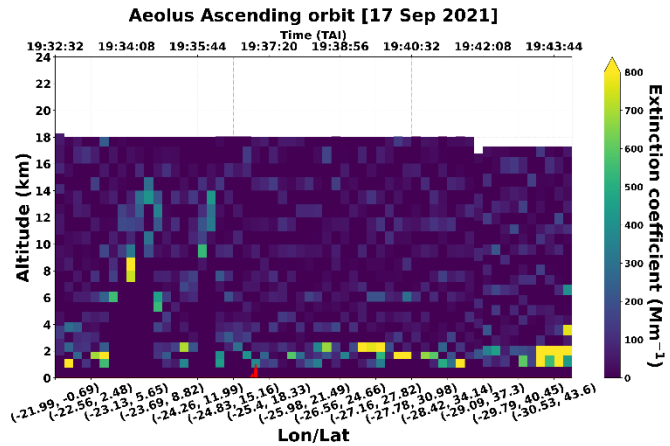


Figure 14: Raw profiles of L2A SCA Mid-Bin extinction coefficient for the Aeolus overpass on 17<sup>th</sup> of September 2021.

|            |  |                        |   |
|------------|--|------------------------|---|
| beta       | $10^{-6} \text{ sr}^{-1} \text{ m}^{-1}$ | 2d<br>(mb-lays, profs) | Particle backscatter coefficient of the middle bin. |
| beta_error | $10^{-6} \text{ sr}^{-1} \text{ m}^{-1}$ | 2d<br>(mb-lays, profs) | Backscatter error                                   |

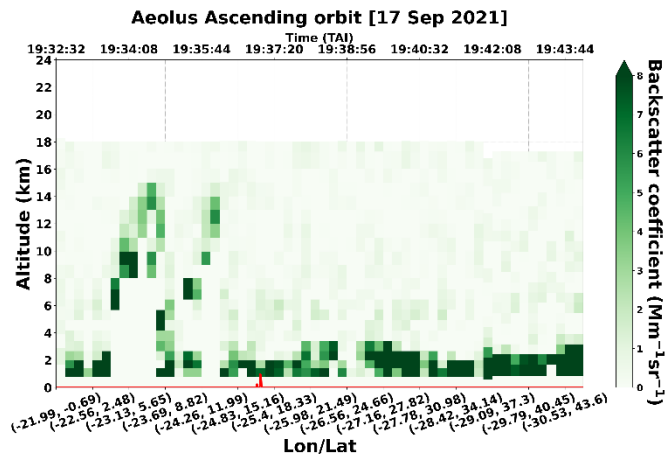


Figure 15: Raw profiles of L2A SCA Mid-Bin backscatter coefficient for the Aeolus overpass on 17<sup>th</sup> of September 2021.

|        |          |                                |   |
|--------|----------|--------------------------------|---|
| lr     | sr       | 2d<br>(mb-lays, profs)         | Particle extinction-to-backscatter ratio of the middle bin. |
| qcflag | No Units | 3d<br>(Qcflags, mblays, profs) | QC information about processing.                            |



|     |            | time                                     | Date format                              | 1d<br>(profs)       | Start date and time of the SCA profile covered by the present DSR. |
|-----|------------|--|--|---------------------|--|
| MLE |            | alpha                                    | $10^{-6} \text{ m}^{-1}$                 | 2d<br>(lays, profs) | Particle extinction coefficient of the bin.                        |
|     |            | alpha_error                              | $10^{-6} \text{ m}^{-1}$                 | 2d<br>(lays, profs) | Extinction error   |
|     |            |  |  |                     |  |
|     |            | beta                                     | $10^{-6} \text{ sr}^{-1} \text{ m}^{-1}$ | 2d<br>(lays, profs) | Particle backscatter coefficient of the bin                        |
|     | beta_error | $10^{-6} \text{ sr}^{-1} \text{ m}^{-1}$ | 2d<br>(lays, profs)                      | Backscatter error   |  |

Figure 16: Raw profiles of L2A MLE extinction coefficient for an indicative Aeolus overpass on 17<sup>th</sup> of September 2021 (orbit id: 017790).



# L2A+

Ref: *Ref: ESA AO/1-11041/22/I-NS*

DI05: Output Data Product (OP)

Page: 36

|                |     |             |  |                     |   |
|----------------|-----|-------------|--|---------------------|---|
|                |     |             |  |                     |   |
| CLOUD-FILTERED | SCA | lr<br>alpha | sr<br>$10^{-6} \text{ m}^{-1}$           | 2d<br>(lays, profs) | Particle extinction-to-backscatter ratio.   |
|                |     | alpha_error | $10^{-6} \text{ m}^{-1}$                 | 2d<br>(lays, profs) | Extinction error                            |
|                |     |             |  |                     |   |
|                |     | beta        | $10^{-6} \text{ sr}^{-1} \text{ m}^{-1}$ | 2d<br>(lays, profs) | Particle backscatter coefficient of the bin |
|                |     | beta_error  | $10^{-6} \text{ sr}^{-1} \text{ m}^{-1}$ | 2d<br>(lays, profs) | Backscatter error                           |

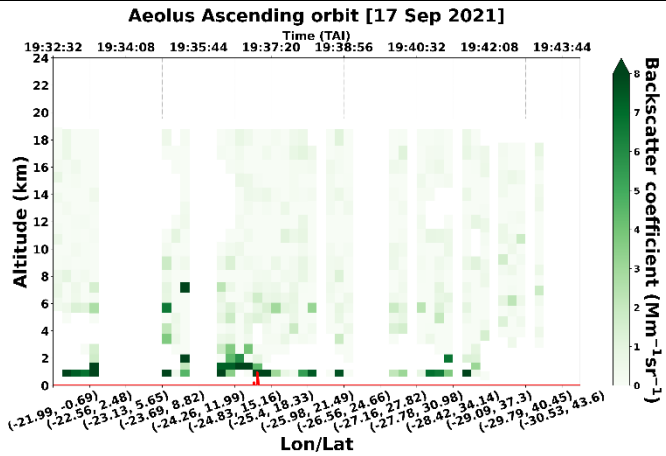


Figure 19: Cloud-filtered profiles of L2A SCA backscatter coefficient.

|             |             |                          |                        |  |
|-------------|-------------|--------------------------|------------------------|--|
|             | lr          | sr                       | 2d<br>(lays, profs)    | Particle extinction-to-backscatter ratio.          |
| SCA_MID_BIN | alpha       | $10^{-6} \text{ m}^{-1}$ | 2d<br>(mb-lays, profs) | Particle extinction coefficient of the middle bin. |
|             | alpha_error | $10^{-6} \text{ m}^{-1}$ | 2d<br>(mb-lays, profs) | Extinction error.                                  |

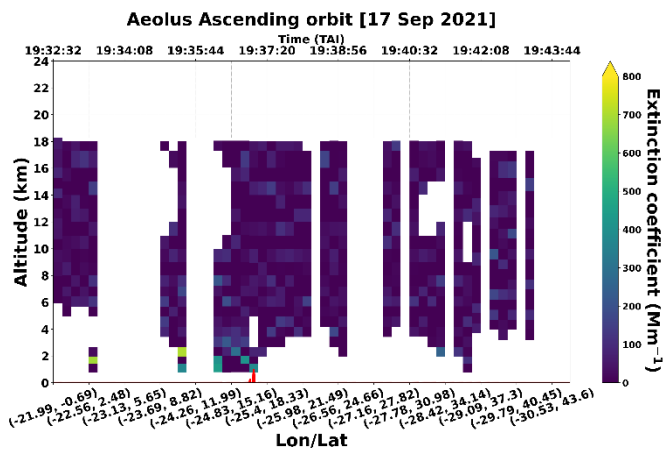


Figure 20: Cloud-filtered profiles of L2A SCA Mid-Bin extinction coefficient.

|  |            |  |                        |   |
|--|------------|--|------------------------|---|
|  | beta       | $10^{-6} \text{ sr}^{-1} \text{ m}^{-1}$ | 2d<br>(mb-lays, profs) | Particle backscatter coefficient of the middle bin. |
|  | beta_error | $10^{-6} \text{ sr}^{-1} \text{ m}^{-1}$ | 2d<br>(mb-lays, profs) | Backscatter error.                                  |

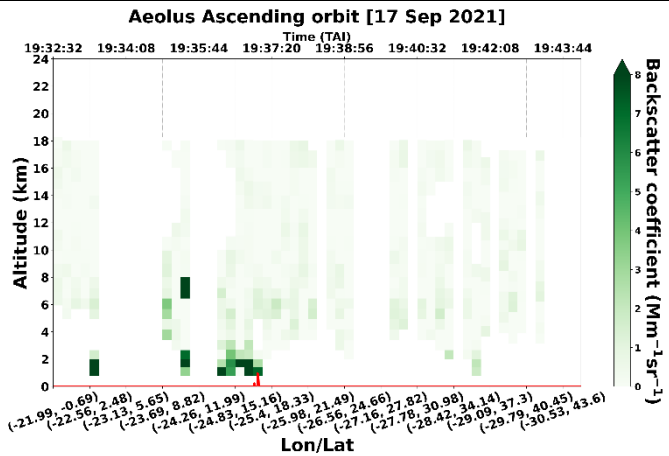


Figure 21: Cloud-filtered profiles of L2A SCA Mid-Bin backscatter coefficient.

|     |             |                          |                        |   |
|-----|-------------|--------------------------|------------------------|---|
|     | lr          | sr                       | 2d<br>(mb-lays, profs) | Particle extinction-to-backscatter ratio of the middle bin. |
| MLE | alpha       | $10^{-6} \text{ m}^{-1}$ | 2d<br>(lays, profs)    | Particle extinction coefficient of the bin.                 |
|     | alpha_error | $10^{-6} \text{ m}^{-1}$ | 2d<br>(lays, profs)    | Extinction error  |

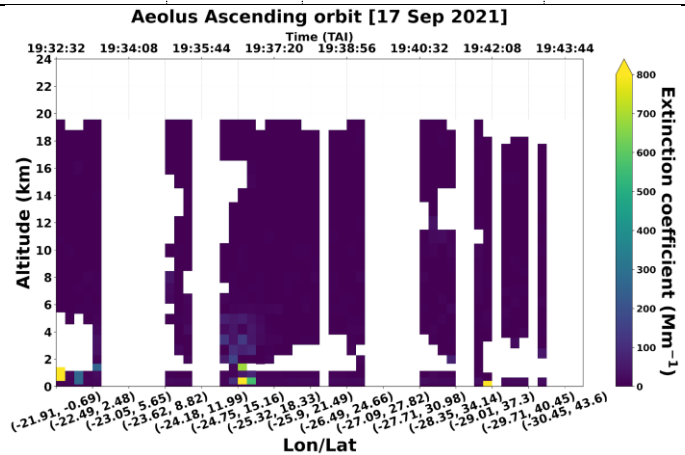


Figure 22: Cloud-filtered profiles of L2A MLE extinction coefficient.

|  |            |  |                     |   |
|--|------------|--|---------------------|---|
|  | beta       | $10^{-6} \text{ sr}^{-1} \text{ m}^{-1}$ | 2d<br>(lays, profs) | Particle backscatter coefficient of the bin |
|  | beta_error | $10^{-6} \text{ sr}^{-1} \text{ m}^{-1}$ | 2d                  | Backscatter error                           |



# L2A+

Ref: *ESA AO/1-11041/22/I-NS*

DI05: Output Data Product (OP)

Page: 39

(lays, profs)

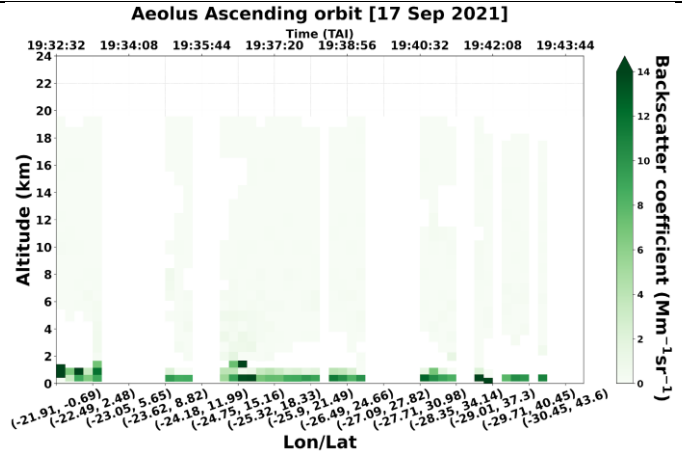


Figure 23: Cloud-filtered profiles of L2A MLE backscatter coefficient.

PURE DUST

SCA

alpha

$10^{-6} \text{ m}^{-1}$

2d

(lays, profs)

Particle extinction coefficient of the bin.

alpha\_error

$10^{-6} \text{ m}^{-1}$

2d

(lays, profs)

Extinction error.

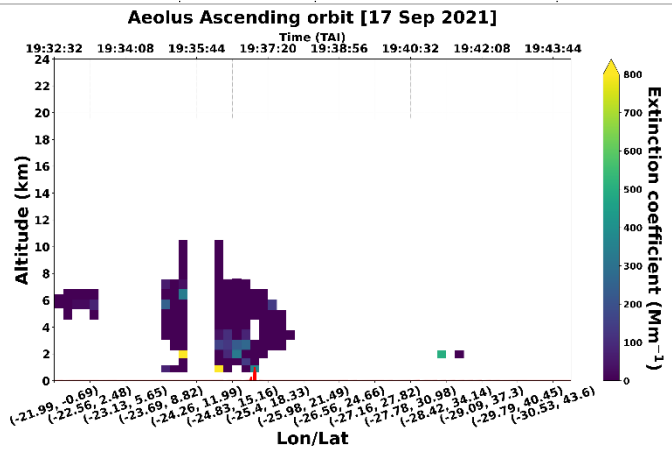


Figure 24: Cloud-free dust profiles of L2A SCA extinction coefficient.

beta

$10^{-6} \text{ sr}^{-1} \text{ m}^{-1}$

2d

(lays, profs)

Particle backscatter coefficient of the bin

beta\_error

$10^{-6} \text{ sr}^{-1} \text{ m}^{-1}$

2d

(lays, profs)

Backscatter error.

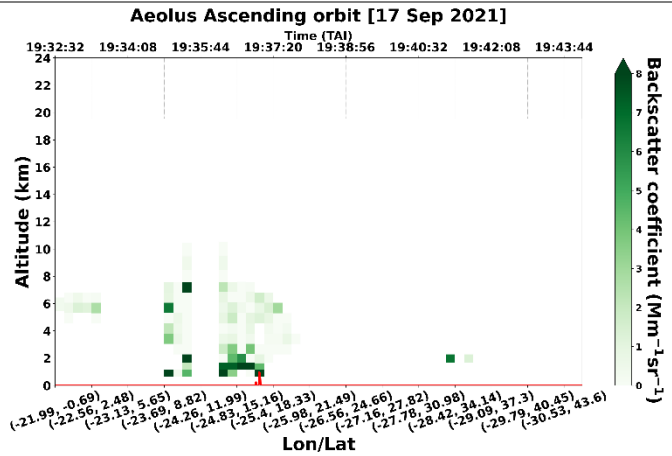


Figure 25: Cloud-free dust profiles of L2A SCA backscatter coefficient.

SCA\_MID\_BIN

|             |                          |                        |  |
|-------------|--------------------------|------------------------|--|
| alpha       | $10^{-6} \text{ m}^{-1}$ | 2d<br>(mb-lays, profs) | Particle extinction coefficient of the middle bin. |
| alpha_error | $10^{-6} \text{ m}^{-1}$ | 2d<br>(mb-lays, profs) | Extinction error.                                  |

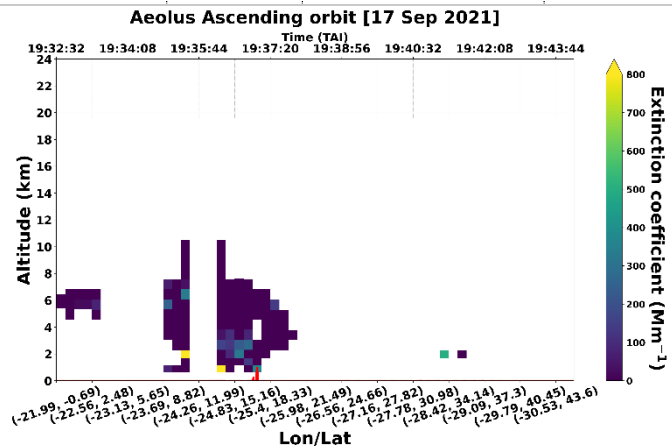


Figure 26: Cloud-free dust profiles of L2A SCA Mid-Bin extinction coefficient.

|            |  |                        |   |
|------------|--|------------------------|---|
| beta       | $10^{-6} \text{ sr}^{-1} \text{ m}^{-1}$ | 2d<br>(mb-lays, profs) | Particle backscatter coefficient of the middle bin. |
| beta_error | $10^{-6} \text{ sr}^{-1} \text{ m}^{-1}$ | 2d<br>(mb-lays, profs) | Backscatter error.                                  |

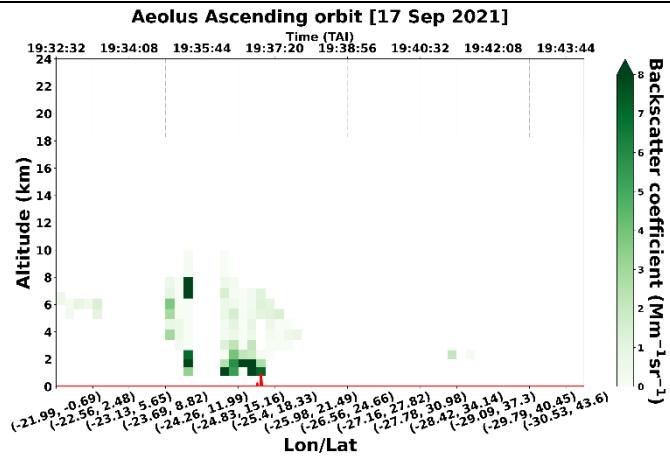


Figure 27: Cloud-free dust profiles of L2A SCA Mid-Bin backscatter coefficient.

MLE

alpha

$10^{-6} \text{ m}^{-1}$

2d  
(lays, profs)

Particle extinction coefficient of the bin.

alpha\_error

$10^{-6} \text{ m}^{-1}$

2d  
(lays, profs)

Extinction error.

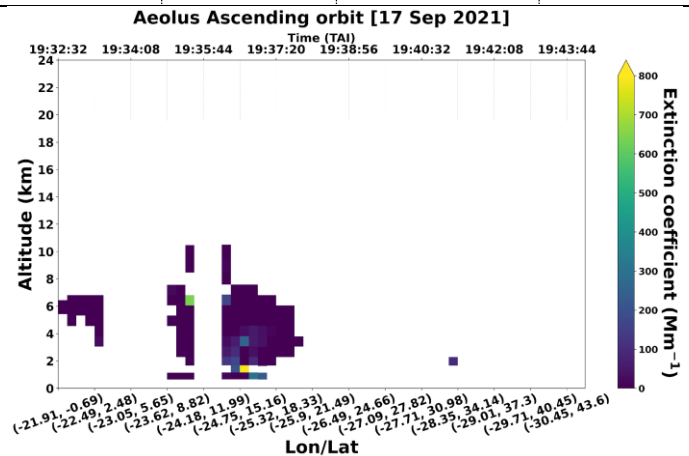


Figure 28: Cloud-free dust profiles of L2A MLE extinction coefficient.

beta

$10^{-6} \text{ sr}^{-1} \text{ m}^{-1}$

2d  
(lays, profs)

Particle backscatter coefficient of the bin

beta\_error

$10^{-6} \text{ sr}^{-1} \text{ m}^{-1}$

2d  
(lays, profs)

Backscatter error.



# L2A+

Ref: *ESA AO/1-11041/22/I-NS*

DI05: Output Data Product (OP)

Page: 42

|         |     |  |  |                     |   |
|---------|-----|--|--|---------------------|---|
|         |     | <p>Figure 29: Cloud-free dust profiles of L2A MLE backscatter coefficient.</p>   |  |                     |   |
| L2APLUS | SCA | beta_co  | 10 <sup>-6</sup> sr <sup>-1</sup><br>m <sup>-1</sup> | 2d<br>(lays, profs) | Co-component of backscatter coefficient.    |
|         |     | <p>Figure 30: Provides the vertical profiles of the co-component of backscatter coefficient along the Aeolus overpass.</p> |  |                     |   |
|         |     | beta_cross   | 10 <sup>-6</sup> sr <sup>-1</sup><br>m <sup>-1</sup> | 2d<br>(lays, profs) | Cross-component of backscatter coefficient. |

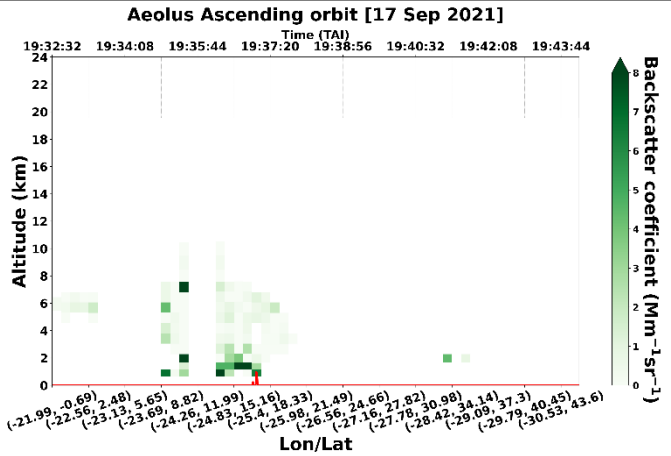


Figure 31: Profiles of the SCA Cross-component backscatter coefficient along the Aeolus overpass (id:017790).

|            |  |                     |                                |
|------------|--|---------------------|--------------------------------|
| beta_total | $10^{-6} \text{ sr}^{-1} \text{ m}^{-1}$ | 2d<br>(lays, profs) | Total backscatter coefficient. |
|------------|--|---------------------|--------------------------------|

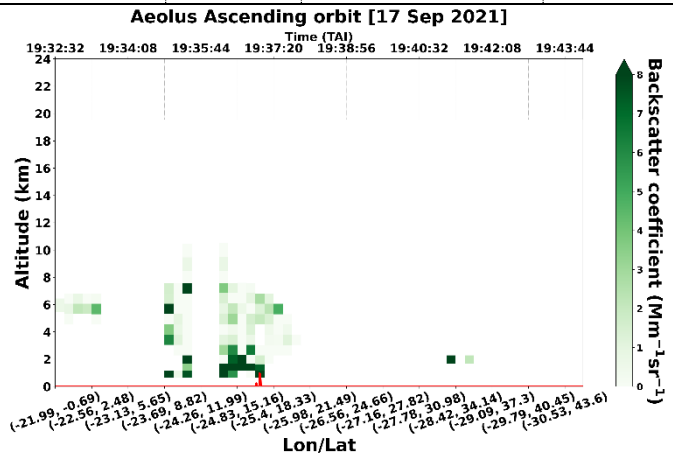


Figure 32: Profiles of the total (co + cross components) SCA backscatter coefficient.

|                |                          |                     |                                       |
|----------------|--------------------------|---------------------|---------------------------------------|
| alpha_plus_355 | $10^{-6} \text{ m}^{-1}$ | 2d<br>(lays, profs) | L2A+ extinction coefficient at 355nm. |
|----------------|--------------------------|---------------------|---------------------------------------|



# L2A+

Ref: *ESA AO/1-11041/22/I-NS*

DI05: Output Data Product (OP)

Page: 44

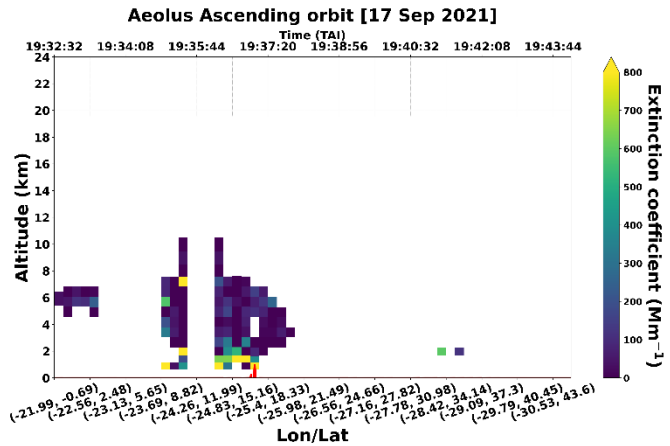


Figure 33: Profiles of the reconstructed L2A+ SCA extinction coefficient at 355nm.

|                |                          |                     |  |
|----------------|--------------------------|---------------------|--|
| alpha_plus_532 | $10^{-6} \text{ m}^{-1}$ | 2d<br>(lays, profs) | L2A+<br>extinction<br>coefficient at<br>532nm. |
|----------------|--------------------------|---------------------|--|

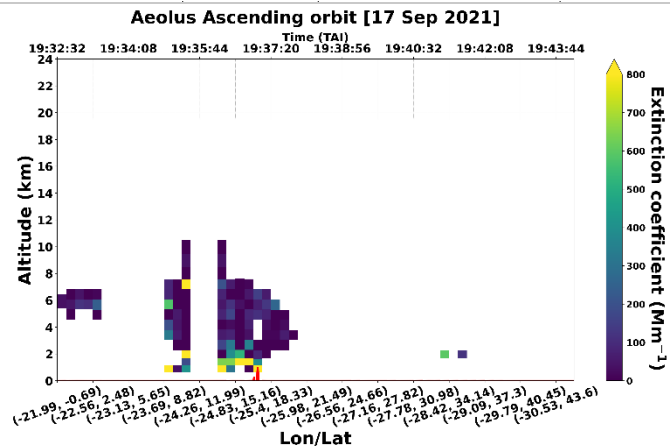


Figure 34: Profiles of the reconstructed L2A+ SCA extinction coefficient at 532nm.

|                |                          |                     |                             |
|----------------|--------------------------|---------------------|-----------------------------|
| dust_concentr. | $\mu\text{g}/\text{m}^3$ | 2d<br>(lays, profs) | Dust mass<br>concentration. |
|----------------|--------------------------|---------------------|-----------------------------|

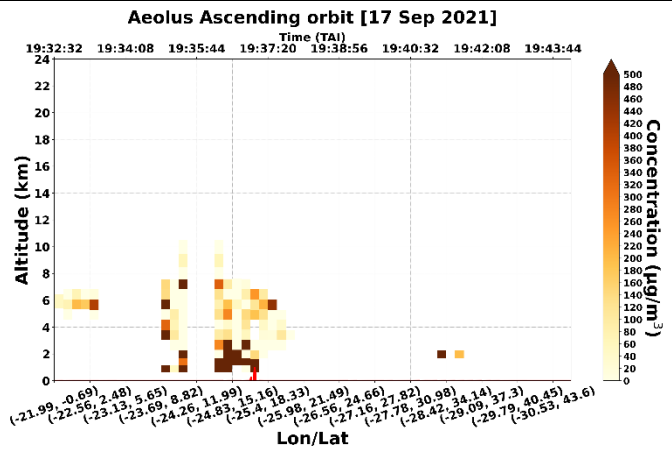


Figure 35: Profiles of the L2A+ dust mass concentration along the Aeolus overpass (id:017790).

SCA\_MID\_BIN

|         |  |                        |   |
|---------|--|------------------------|---|
| beta_co | $10^{-6} \text{ sr}^{-1} \text{ m}^{-1}$ | 2d<br>(mb-lays, profs) | Co-component of backscatter coefficient at 355nm. |
|---------|--|------------------------|---|

See Figure 13 which gives vertical profiles of the co-component of backscatter coefficient at Mid-Bin scale along the Aeolus overpass.

|            |  |                        |   |
|------------|--|------------------------|---|
| beta_cross | $10^{-6} \text{ sr}^{-1} \text{ m}^{-1}$ | 2d<br>(mb-lays, profs) | Cross-component of backscatter coefficient at 355 nm. |
|------------|--|------------------------|---|

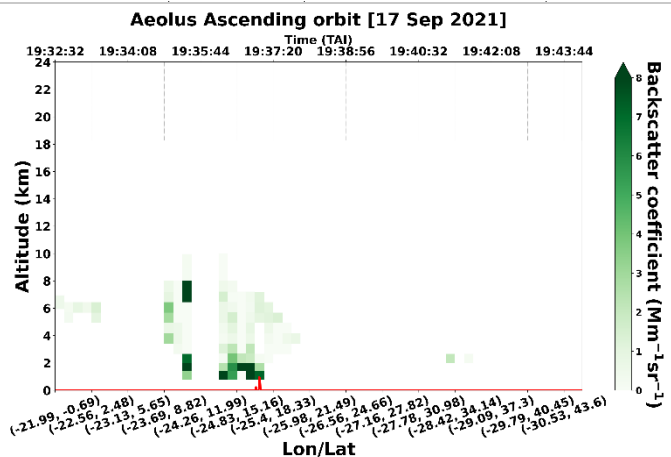


Figure 36: Profiles of the SCA Mid-Bin Cross-component backscatter coefficient along the Aeolus overpass (id:017790).

|            |  |                        |   |
|------------|--|------------------------|---|
| beta_total | $10^{-6} \text{ sr}^{-1} \text{ m}^{-1}$ | 2d<br>(mb-lays, profs) | Total backscatter coefficient at 355nm. |
|------------|--|------------------------|---|



# L2A+

Ref: *ESA AO/1-11041/22/I-NS*

DI05: Output Data Product (OP)

Page: 46

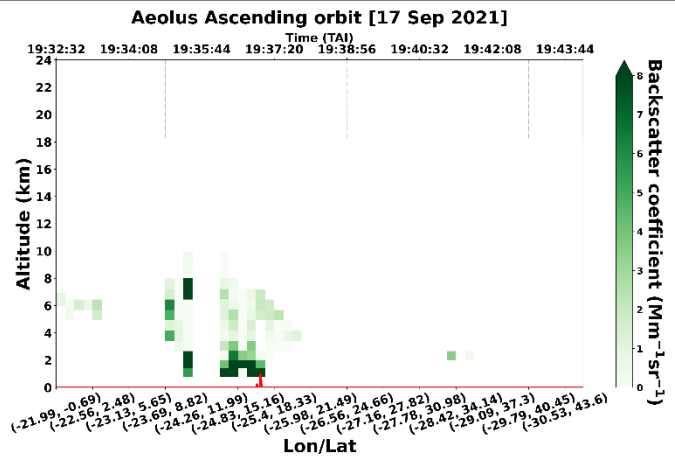


Figure 37: Profiles of the total (co + cross components) SCA Mid-Bin backscatter coefficient.

|                |                          |                        |  |
|----------------|--------------------------|------------------------|--|
| alpha_plus_355 | $10^{-6} \text{ m}^{-1}$ | 2d<br>(mb-lays, profs) | L2A+<br>extinction<br>coefficient at<br>355nm. |
|----------------|--------------------------|------------------------|--|

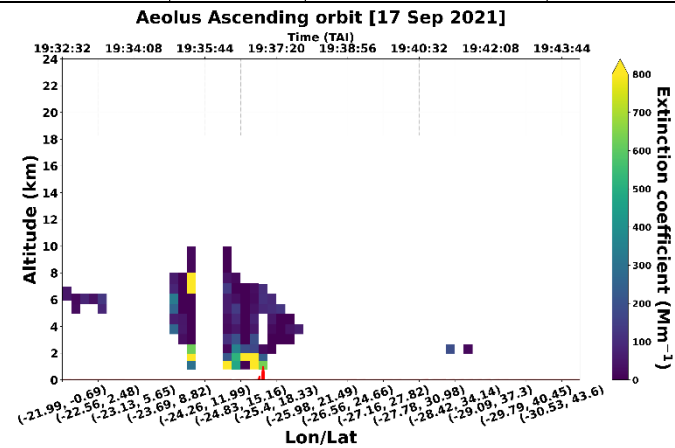


Figure 38. Profiles of the reconstructed L2A+ SCA Mid-Bin extinction coefficient at 355nm.

|                |                          |                        |  |
|----------------|--------------------------|------------------------|--|
| alpha_plus_532 | $10^{-6} \text{ m}^{-1}$ | 2d<br>(mb-lays, profs) | L2A+<br>extinction<br>coefficient at<br>532nm. |
|----------------|--------------------------|------------------------|--|



# L2A+

Ref: *Ref: ESA AO/1-11041/22/I-NS*

DI05: Output Data Product (OP)

Page: 47

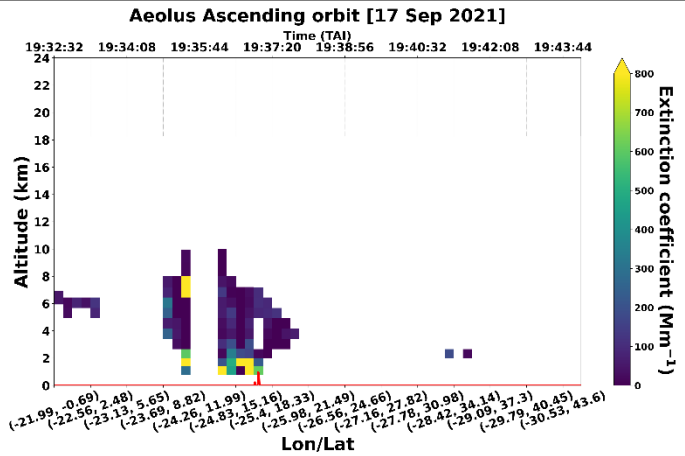


Figure 39. Profiles of the reconstructed L2A+ SCA Mid-Bin extinction coefficient at 532nm.

|                |                          |                  |                          |
|----------------|--------------------------|------------------|--------------------------|
| dust_concentr. | $\mu\text{g}/\text{m}^3$ | 2d               | Dust mass concentration. |
|                |                          | (mb-lays, profs) |                          |

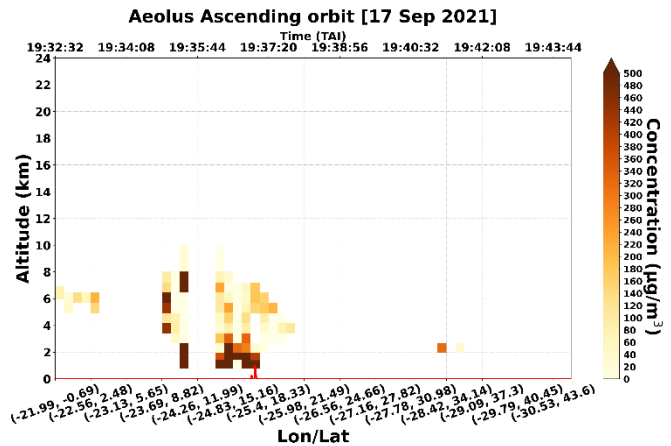


Figure 40: Profiles of the L2A+ dust mass concentration at Mid-Bin scale along the Aeolus overpass (id:017790).

|     |         |  |               |  |
|-----|---------|--|---------------|--|
| MLE | beta_co | $10^{-6} \text{ sr}^{-1} \text{ m}^{-1}$ | 2d            | Co-component of backscatter coefficient. |
|     |         |  | (lays, profs) |  |

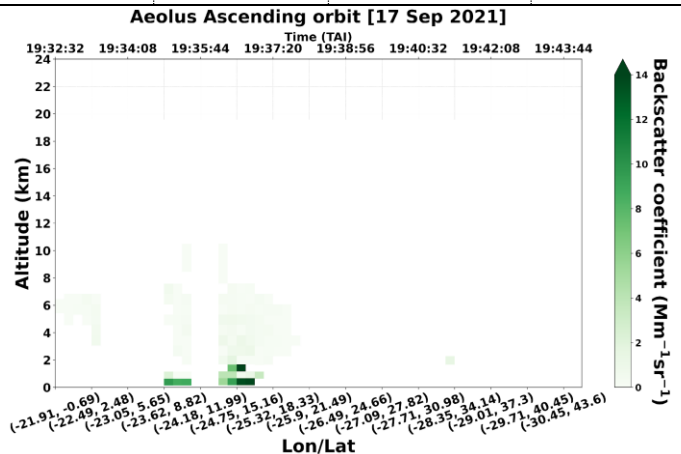




Figure 41: Vertical profiles of the MLE co-component of backscatter coefficient along the Aeolus overpass.

|            |  |                     |   |
|------------|--|---------------------|---|
| beta_cross | $10^{-6} \text{ sr}^{-1} \text{ m}^{-1}$ | 2d<br>(lays, profs) | Cross-component of backscatter coefficient. |
|------------|--|---------------------|---|

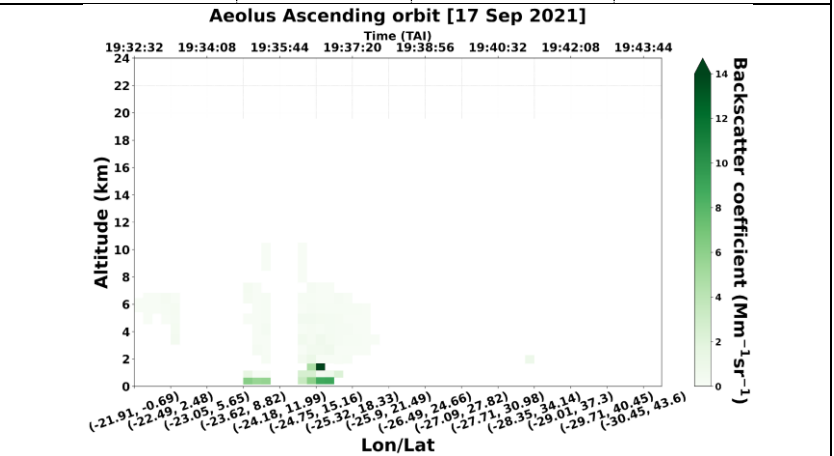


Figure 42: Profiles of the MLE Cross-component backscatter coefficient along the Aeolus overpass (id:017790).

|            |  |                     |                                |
|------------|--|---------------------|--------------------------------|
| beta_total | $10^{-6} \text{ sr}^{-1} \text{ m}^{-1}$ | 2d<br>(lays, profs) | Total backscatter coefficient. |
|------------|--|---------------------|--------------------------------|

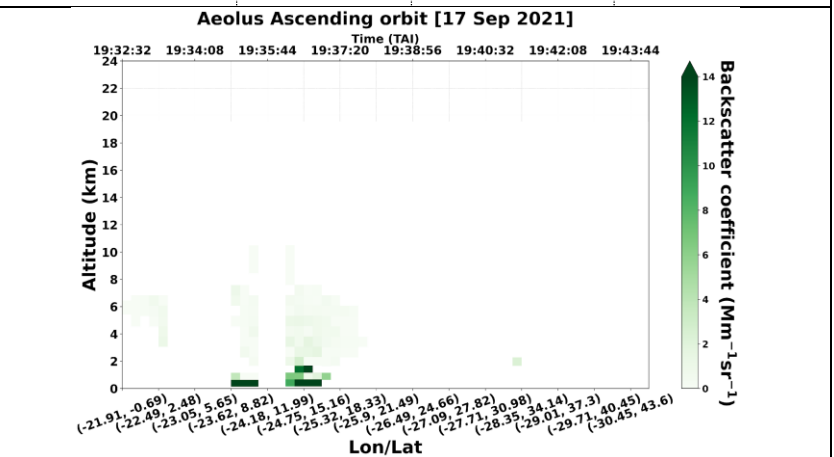


Figure 43: Profiles of the total (co + cross components) MLE backscatter coefficient.

|                |                          |                     |                                       |
|----------------|--------------------------|---------------------|---------------------------------------|
| alpha_plus_355 | $10^{-6} \text{ m}^{-1}$ | 2d<br>(lays, profs) | L2A+ extinction coefficient at 355nm. |
|----------------|--------------------------|---------------------|---------------------------------------|



# L2A+

Ref: *ESA AO/1-11041/22/I-NS*

DI05: Output Data Product (OP)

Page: 49

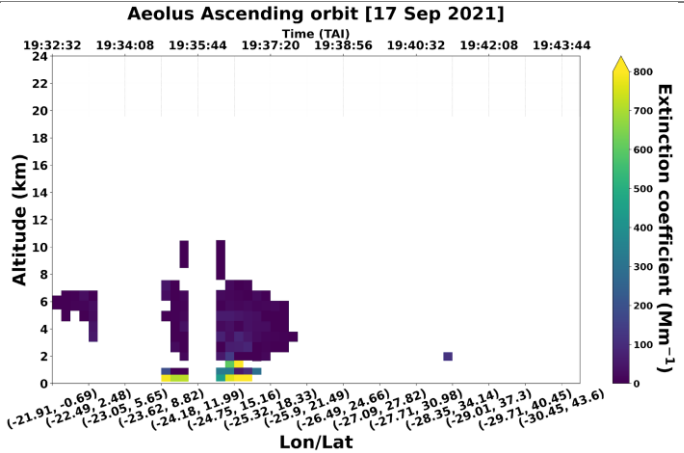


Figure 44. Profiles of the reconstructed L2A+ MLE extinction coefficient at 355nm.

|                |                          |                     |  |
|----------------|--------------------------|---------------------|--|
| alpha_plus_532 | $10^{-6} \text{ m}^{-1}$ | 2d<br>(lays, profs) | L2A+<br>extinction<br>coefficient at<br>532nm. |
|----------------|--------------------------|---------------------|--|

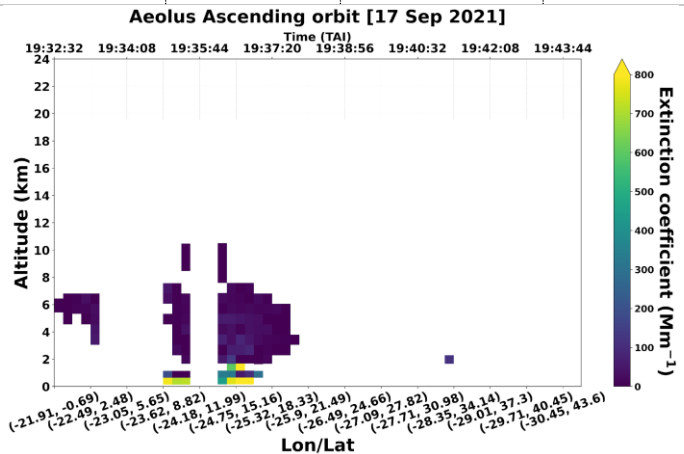


Figure 45. Profiles of the reconstructed L2A+ MLE extinction coefficient at 532nm.

|                |                          |                     |                             |
|----------------|--------------------------|---------------------|-----------------------------|
| dust_concentr. | $\mu\text{g}/\text{m}^3$ | 2d<br>(lays, profs) | Dust mass<br>concentration. |
|----------------|--------------------------|---------------------|-----------------------------|

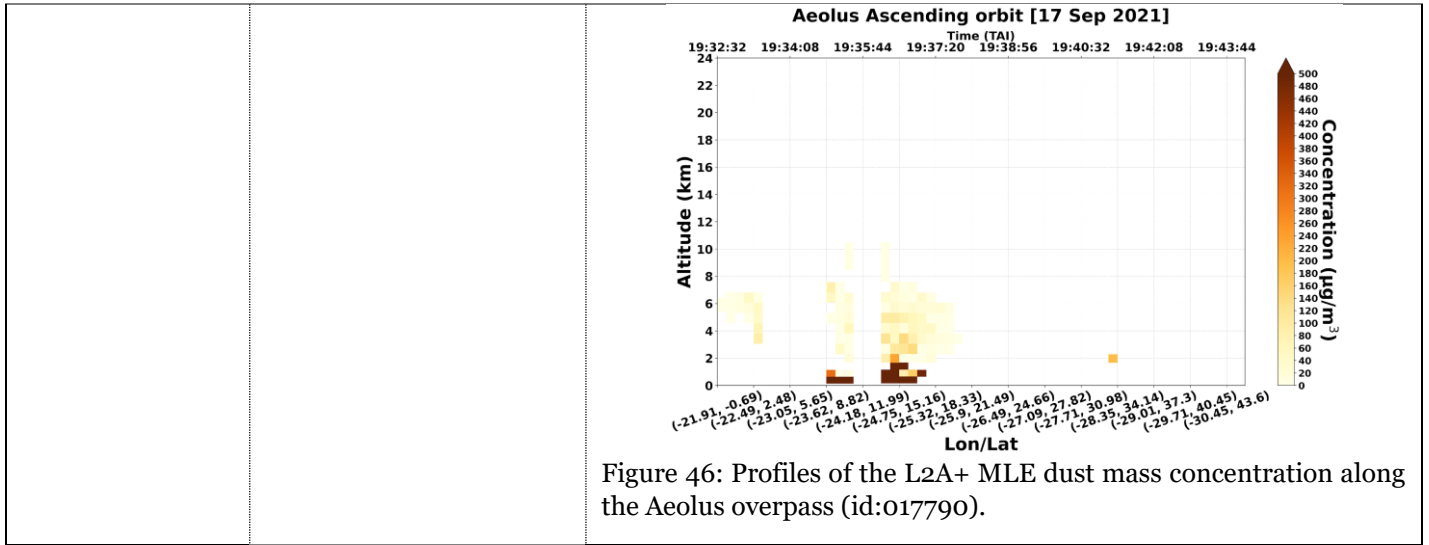


# L2A+

Ref: Ref: ESA AO/1-11041/22/I-NS

DI05: Output Data Product (OP)

Page: 50



| Name  | Long Name  | Type       |
|---|--|------------|
| AE_OPER_ALD_U_N_2A_20210910T181932020_00... | AE_OPER_ALD_U_N_2A_20210910T181932020_008508008... | Local File |
| ▼ CLOUD_FILTERED                            | CLOUD_FILTERED                                     | —          |
| ▶ MLE                                       | MLE  | —          |
| ▶ SCA                                       | SCA  | —          |
| ▶ SCA_MID_BIN                               | SCA_MID_BIN  | —          |
| ▼ GEOLOCATION                               | GEOLOCATION  | —          |
| ▶ DEM_INTERSECTION                          | DEM_INTERSECTION                                   | —          |
| ▶ MIDDLE_BIN_SCALE                          | MIDDLE_BIN_SCALE                                   | —          |
| ▶ REGULAR_SCALE                             | REGULAR_SCALE                                      | —          |
| ▼ L2APLUS                                   | L2APLUS  | —          |
| ▼ MLE                                       | MLE  | —          |
| alpha_plus_355                              | L2A+ extinction coefficient at 355nm               | 2D         |
| alpha_plus_532                              | L2A+ extinction coefficient at 532nm               | 2D         |
| beta_co                                     | Co-component of backscatter coefficient            | 2D         |
| beta_cross                                  | Cross-component of backscatter coefficient         | 2D         |
| beta_total                                  | Total backscatter coefficient                      | 2D         |
| dust_concentration                          | Dust mass concentration                            | 2D         |
| ▶ SCA                                       | SCA  | —          |
| ▶ SCA_MID_BIN                               | SCA_MID_BIN  | —          |
| ▼ PURE_DUST                                 | PURE_DUST  | —          |
| ▶ MLE                                       | MLE  | —          |
| ▶ SCA                                       | SCA  | —          |
| ▶ SCA_MID_BIN                               | SCA_MID_BIN  | —          |
| ▼ RAW_DATA                                  | RAW_DATA   | —          |
| ▶ MLE                                       | MLE  | —          |
| ▶ SCA                                       | SCA  | —          |
| ▶ SCA_MID_BIN                               | SCA_MID_BIN  | —          |

Figure 47: Indicative file output of the L2A/L2A+ optical properties.



# L2A+

Ref: *Ref: ESA AO/1-11041/22/I-NS*

DI05: Output Data Product (OP)

Page: 51

## 3.5. Access Credentials

Access to the ESA-L2A+ products are provided according to the following access credentials:

Table 6: ESA-L2A+ WP3000 access credentials.

| L2A+ OPs  |                    |
|-----------|--------------------|
| Protocol: | SFTP (Port 22)     |
| Username: | l2aplus_wp2000     |
| Password: | eYst5kuxngzn       |
| Host:     | react.space.noa.gr |

## 3.6. Contact Person

### Contact:

Users can contact with Konstantinos Rizos ([k.rizos@noa.gr](mailto:k.rizos@noa.gr)) for any further details and clarifications regarding the L2A+ dataset.



# L2A+

Ref: Ref: ESA AO/1-11041/22/I-NS

DI05: Output Data Product (OP)

Page: 52

## Acronyms and Abbreviations

|             |   |
|-------------|---|
| L2A         | Aeolus Level 2A product                                     |
| L2A+        | Improved Aeolus Level 2A product                            |
| SCA         | Standard Correct Algorithm                                  |
| SCA_MID_BIN | Standard Correct Algorithm at the Middle-Bin vertical scale |

## List of Figures

| Figure | Description   |
|--------|---|
| 01     | ESA-L2A+ WP2000, WP3000, and WP4000 input and outputs relevant to DI05  |
| 02     | Indicative file output of Unique feature mask over Mindelo.   |
| 03     | Indicative file output of PollyXT optical properties.   |
| 04     | a) Aeolus ascending orbit (id: 017679) over the L2A+ RoI on 10th September 2021 and b) the time-closest spatial distribution of clouds derived from the binary cloud-mask product of MSG-SEVIRI CLAAS-3 dataset   |
| 05     | a) AEL-FM feature mask product along the Aeolus orbit (id: 017679) on 10th September 2021 and the transformed feature mask product on the Aeolus vertical and horizontal resolution for the b) regular (24 bins) and c) middle-bin scale (23 bins).   |
| 06     | Vertical profiles of CAMS dust mass concentration and dust-to-total aerosol mass concentration ratio along the Aeolus orbit (id: 017679) provided in the regular (a, b) and middle-bin (c, d) vertical scales on the 10th of September 2021.  |
| 07     | (a) CALIPSO total backscatter coefficient at 532 nm. (b) CALIPSO particulate depolarization ratio at 532 nm (c) CALIPSO QA pure-aerosol total backscatter coefficient at 532 nm (d) CALIPSO QA pure-dust backscatter coefficient at 532 nm.   |
| 08     | Raw Aeolus L2A backscatter profiles at 355 nm along the Aeolus orbit (id 017679) retrieved from the SCA, SCA mid-bin and MLE algorithms (left panel) and the corresponding QA pure-aerosol backscatter profiles at 355 nm for the SCA, SCA mid-bin and MLE algorithms (right panel).  |
| 09     | Co-polar and cross polar backscatter profiles along the Aeolus overpass (id 017679) for the SCA (a, b) and SCA mid-bin algorithms (c, d).   |
| 10     | Vertical profiles of the raw Aeolus L2A and QA L2A+ backscatter coefficient at 355 nm retrieved from the SCA, SCA mid-bin and MLE algorithms with the corresponding backscatter profiles at 355 nm acquired by eVe ground-based lidar (left panel), and QA Aeolus L2A and L2A+ backscatter profiles for the SCA, SCA mid-bin and MLE algorithms with the derived backscatter profiles from eVe lidar (right panel).         |
| 11     | Vertical profiles of the raw Aeolus L2A and QA L2A+ backscatter coefficient at 355 nm retrieved from the SCA, SCA mid-bin and MLE algorithms with the corresponding backscatter profiles at 355 nm acquired by PollyXT ground-based lidar (left panel), and QA Aeolus L2A and L2A+ backscatter profiles for the SCA, SCA mid-bin and MLE algorithms with the derived backscatter profiles from PollyXT lidar (right panel). |
| 12     | Raw profiles of L2A SCA extinction coefficient for an indicative Aeolus overpass on 17th of September 2021 (orbit id: 017790).  |
| 13     | Raw profiles of L2A SCA backscatter coefficient for the Aeolus overpass on 17th of September 2021.  |
| 14     | Raw profiles of L2A SCA Mid-Bin extinction coefficient for the Aeolus overpass on 17th of September 2021.   |



# L2A+

Ref: Ref: ESA AO/1-11041/22/I-NS

DI05: Output Data Product (OP)

Page: 53

|    |  |
|----|--|
| 15 | Raw profiles of L2A SCA Mid-Bin backscatter coefficient for the Aeolus overpass on 17th of September 2021.                     |
| 16 | Raw profiles of L2A MLE extinction coefficient for an indicative Aeolus overpass on 17th of September 2021 (orbit id: 017790). |
| 17 | Raw profiles of L2A MLE backscatter coefficient for the Aeolus overpass on 17th of September 2021.                             |
| 18 | Cloud-filtered profiles of L2A SCA extinction coefficient.   |
| 19 | Cloud-filtered profiles of L2A SCA backscatter coefficient.  |
| 20 | Cloud-filtered profiles of L2A SCA Mid-Bin extinction coefficient.   |
| 21 | Cloud-filtered profiles of L2A SCA Mid-Bin backscatter coefficient.  |
| 22 | Cloud-filtered profiles of L2A MLE extinction coefficient.   |
| 23 | Cloud-filtered profiles of L2A MLE backscatter coefficient.  |
| 24 | Cloud-free dust profiles of L2A SCA extinction coefficient.  |
| 25 | Cloud-free dust profiles of L2A SCA backscatter coefficient.   |
| 26 | Cloud-free dust profiles of L2A SCA Mid-Bin extinction coefficient.  |
| 27 | Cloud-free dust profiles of L2A SCA Mid-Bin backscatter coefficient.   |
| 28 | Cloud-free dust profiles of L2A MLE extinction coefficient.  |
| 29 | Cloud-free dust profiles of L2A MLE backscatter coefficient.   |
| 30 | Provides the vertical profiles of the co-component of backscatter coefficient along the Aeolus overpass.                       |
| 31 | Profiles of the SCA Cross-component backscatter coefficient along the Aeolus overpass (id:017790).                             |
| 32 | Profiles of the total (co + cross components) SCA backscatter coefficient.   |
| 33 | Profiles of the reconstructed L2A+ SCA extinction coefficient at 355nm.  |
| 34 | Profiles of the reconstructed L2A+ SCA extinction coefficient at 532nm.  |
| 35 | Profiles of the L2A+ dust mass concentration along the Aeolus overpass (id:017790).  |
| 36 | Profiles of the SCA Mid-Bin Cross-component backscatter coefficient along the Aeolus overpass (id:017790).                     |
| 37 | Profiles of the total (co + cross components) SCA Mid-Bin backscatter coefficient.   |
| 38 | Profiles of the reconstructed L2A+ SCA Mid-Bin extinction coefficient at 355nm.  |
| 39 | Profiles of the reconstructed L2A+ SCA Mid-Bin extinction coefficient at 532nm.  |
| 40 | Profiles of the L2A+ dust mass concentration at Mid-Bin scale along the Aeolus overpass (id:017790).                           |
| 41 | Vertical profiles of the MLE co-component of backscatter coefficient along the Aeolus overpass.                                |
| 42 | Profiles of the MLE Cross-component backscatter coefficient along the Aeolus overpass (id:017790).                             |
| 43 | Profiles of the total (co + cross components) MLE backscatter coefficient.   |
| 44 | Profiles of the reconstructed L2A+ MLE extinction coefficient at 355nm.  |
| 45 | Profiles of the reconstructed L2A+ MLE extinction coefficient at 532nm.  |
| 46 | Profiles of the L2A+ MLE dust mass concentration along the Aeolus overpass (id:017790).  |
| 47 | Indicative file output of the L2A/L2A+ optical properties.   |



# L2A+

Ref: *Ref: ESA AO/1-11041/22/I-NS*

DI05: Output Data Product (OP)

Page: 54

## List of Tables

| Table | Description  |
|-------|--|
| 01    | Provides the vertical profiles of the co-component of backscatter coefficient along the Aeolus overpass. |
| 02    | Detailed description of the variables within the PollyXT profile product.                                |
| 03    | ESA L2A+ WP2000 access credentials.  |
| 04    | L2A+ filename descriptor.  |
| 05    | Detailed description of the groups and variables of the final output L2A+ product.                       |
| 06    | ESA-L2A+ WP3000 access credentials.  |



*L2A+*

Ref: *Ref: ESA AO/1-11041/22/I-NS*

DI05: Output Data Product (OP)

Page: 55

[End of ESA-L2A+ DI05 - OP]